Institute for
Communications
and Navigation

GPS/INS Tightly coupled position and attitude determination with low-cost sensors
Master Thesis

Michele Iafrancesco

Institute for Communications and Navigation

Prof. Dr. Christoph Günther

Supervised by Dr. Patrick Henkel

Munich, September 2015

Institute for Communications and Navigation

Technische Universität München
Theresienstrasse 90
80333 Munich

Abstract

A precise position and attitude information is essential for autonomous driving of vehicles. Until today, many effort has been done to provide such a solution. The most common approach consists of a sensor fusion of GNSS (Global Navigation Satellite System) and INS (Inertial Navigation System) techniques.

GNSS may provide accurate position information, but suffers from signal reflection errors and from signal track losses in deep urban environments. INS in contrast is totally independent from the environment but has a relatively bad long-term accuracy. For this reason, the two approaches are often combined in order to raise the strengths and get rid of the weaknesses of the two individual techniques.

In this work, a Kalman Filter (KF) based tightly coupled position and attitude determination algorithm is developed for two low-cost GNSS receivers, a gyroscope and an accelerometer. In addition, we perform real-time kinematics (RTK) positioning using data from a virtual reference station (VRS) to augment position accuracy.

We demonstrate that, in favorable conditions, we are able to determine the relative position between using carrier phase measurements from two low-cost GNSS receivers achieving centimeter level accuracy. In addition, the measurement model of the inertial sensor was improved, enabling a heading angle estimation with an accuracy of less than one degree with a probability of 99,7% (3σ).

Contents

1 Introduction **1**

2 Coordinate frame parametrization **3**
- 2.1 Coordinate frames . . . 3
  - 2.1.1 Earth-centered earth-fixed coordinate frame . . . 3
  - 2.1.2 Navigation coordinate frame . . . 4
  - 2.1.3 Body-fixed coordinate frame . . . 5
- 2.2 Coordinate frame transformations . . . 5
  - 2.2.1 Attitude parametrization using Euler angles . . . 5
  - 2.2.2 Transformation from the navigation frame to the earth-centered earth-fixed frame . . . 6
  - 2.2.3 Transformation from the body frame to the navigation frame . . . 7
- 2.3 Time derivative of rotating quantities . . . 8
- 2.4 Transformation of the sensed angular rates into the Euler attitude angles . . . 9
- 2.5 Relative motion kinematics . . . 10

3 The Inertial Navigation System **12**
- 3.1 The inertial measurement unit (IMU) . . . 12
  - 3.1.1 Movement model . . . 13
  - 3.1.2 Measurement model . . . 14
- 3.2 INS Mechanization . . . 15
  - 3.2.1 INS Mechanization in the Earth-centered Earth-fixed frame 15

4 The Global Positioning System **17**
- 4.1 Measurement models . . . 18
  - 4.1.1 The pseudorange measurement . . . 18
  - 4.1.2 The carrier phase measurement . . . 18
  - 4.1.3 The Doppler frequency measurement . . . 18
- 4.2 Single and double differences . . . 19
- 4.3 Clock synchronization corrections . . . 20
- 4.4 Integer ambiguity resolution . . . 20

5 Sensor Fusion: The extended Kalman Filter **23**
5.1 Sensor set-up 24
5.2 KF Modeling 25
5.2.1 State transition model 25
5.2.2 Measurement model 28
5.3 The Kalman Filter algorithm 31
5.3.1 The prediction step 31
5.3.2 The update step 32

6 Own contributions and measurement results **34**
6.1 Improvements on static RTK positioning 34
6.1.1 GNSS measurement set-up 34
6.1.2 Fixing algorithm description 35
6.1.3 Fixing algorithm results 39
6.2 Refinements on the inertial sensor model 44
6.2.1 Calibration and first-order bias estimation 44
6.2.2 Improvements on the mathematical model 46
6.2.3 Corrections due to displacement and misalignment of GNSS-centered and INS-centered body frame 53
6.3 Tight coupling results 56

A Nomenclature **61**
A.1 Basic Quantities and Physics 61
A.2 Vectors, Matrices 61
A.3 Positioning 62
A.4 Random Variables, Estimation 62
A.5 Signal Processing 63

Bibliography **63**

Chapter 1

Introduction

The concept of autonomous driving has become more and more a central topic for the automobile industry. The recent developments in sensor fusion techniques will open soon a market sector that could become very valuable. Apart of laser beam imaging techniques for obstacle avoidance, a good part of the research efforts are focusing on visual navigation techniques for positioning purposes. However, the main drawback of visual navigation is the need of mapping data for image georeferentiation. In this sense, the use of positioning techniques that are independent from the environment like Global Navigation Satellite Systems (GNSSi) and Inertial Navigation Systems (INS) can offer a solution that is robust to unpredictable modifications in the surroundings where the positioning shall take place.

Nevertheless, using only one of the just mentioned navigation techniques would not be sufficient to provide continuous and reliable position estimation. Although GNSS may provide accurate position information, it suffers from reduced reliability and continuity issues in case of reduced sky visibility and/or in case of high amount of signal reflectors. On the other hand, INS-based navigation lacks in long term accuracy but ensures high reliability and benefits from being totally autonomous. For this reason, the two navigation techniques are combined in order to raise the strengths and get rid of the weaknesses of the two individual approaches.

In this thesis, a tightly coupled GNSS/INS position and attitude determination algorithm has been further developed. In particular, the research has been focused on the inertial sensor's mathematical model and on the candidate evaluation of the GNSS double differenced carrier phase integer ambiguity fixing algorithm.

The developed algorithm relies on an extended Kalman Filter (KF) and the sensor coupling is performed on measurement level. The filter is updated using the actual GNSS or INS measurement sample. The navigation related estimated parameters are: position, velocity, acceleration, attitude and attitude rate of the vehicle. Moreover, other non-navigational parameters like GNSS single differenced code phase multipath error or INS angular rate and acceleration bias error are continuously estimated, too.

The measurements were taken using both GNSS and INS low-cost sensors. The GNSS related measurements have been recorded using low-cost u-blox patch antennas and single-frequency receivers, whereas the INS consists of a microelectromechanical system (MEMS) inertial measurement unit (IMU). Both sensors benefit from their low cost, weight and power consumption. However, they suffer from various errors which are not negligible: GNSS patch antennas can suffer from severe code phase and also carrier phase multipath errors, single-frequency receivers may suffer from frequent carrier phase cycle slips and, in contrast to dual-frequency receivers, are not able to eliminate atmospheric errors. In addition, the performance of MEMS IMUs degrades quickly over time, which may induce large error during complete GNSS signal outages.

In order to perform precise attitude estimation, a dual antenna set-up has been considered, where two GNSS antennas are mounted on the vehicle's rooftop to get an INS independent attitude estimation, which is also used to initialize the inertial sensors. Furthermore, the absolute position accuracy is augmented using a real time kinematics (RTK) approach, in which the vehicle is positioned relatively to a virtual reference station (VRS). By knowing the position of the VRS, the vehicle can be positioned absolutely, too. In the positioning algorithm, we strongly rely on carrier phase positioning which, thanks to its low noise characteristics, may enable centimeter-level positioning.

The rest of this work is organized as follows: in chapter 2, a brief introduction on the essential navigation related mathematics is presented. Moreover, the INS and GPS navigation techniques are briefly introduced in chapters 3 and 4, respectively, whereas the sensor fusion algorithm, including the definition of our mathematical models are outlined in chapter 5. Finally, the enhancements that have been developed in this thesis are presented, together with the respective results, in chapter 6.

Chapter 2

Coordinate frame parametrization

2.1 Coordinate frames

In order to describe the position and attitude of the vehicle, one has to define a coordinate frame in which the values are referred to. In case of GPS a coordinate frame which is earth ellipsoid referenced is usually chosen, whereas in case of IMU and strapdown mechanization, a coordinate frame that is centered and aligned with the sensor platform is considered. If one considers to perform a coupling of both sensors, one has to choose a common reference coordinate frame in which the estimate is finally outputted. In the following, a brief description of the coordinate frames and their respective transformation techniques are briefly presented. Throughout this section, we refer to [1, 2]

2.1.1 Earth-centered earth-fixed coordinate frame

The Earth-centered earth-fixed coordinate frame, depicted in Figure 2.1, is where, in our model, we express the position, velocity and acceleration vector of the vehicle. This frame is mostly used in GPS, because of its convenient definition. It's an orthogonal right-handed coordinate frame which has its origin fixed in the center of the ellipsoid on which the earth's surface is modeled, and it is earth-fixed: that means that it rotates with the earth itself on the same rotation axis. The z-axis is so oriented to be along to the earth's rotation axis from the center to the Conventional Terrestrial Pole (CTP). The x-axis points from the center to the intersection of the equator with the Greenwich meridian, which defines the zero degree latitude. The y-axis completes the orthogonal set, pointing from the equator to the intersection between the equator and the 90 degree east meridian.

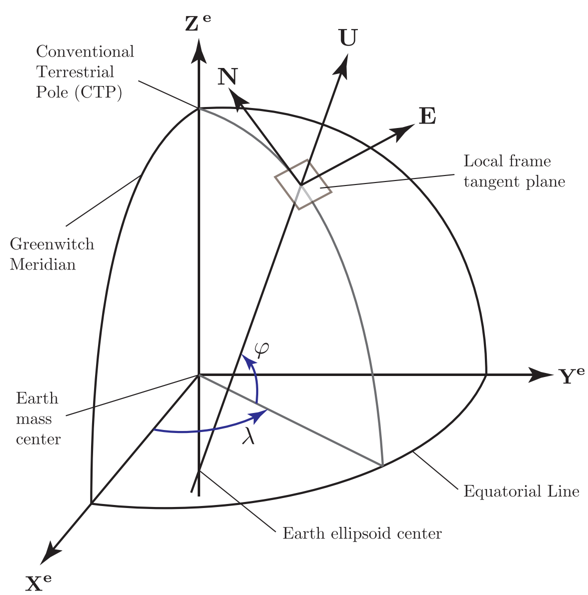

Figure 2.1: Illustration of the Earth-centered-Earth-fixed (ECEF) and East-North-UP (ENU) coordinate frames

2.1.2 Navigation coordinate frame

The navigation coordinate frame, also called local navigation or local-level frame, is always centered in the point for which the navigation solution is sought for (i.e. the vehicle's first GNSS antenna in our case). As can be seen in Figure 2.1, its orientation can be defined in several ways: If one takes the plane that is tangent to the earth's ellipsoid in the origin point, the y-axis is usually defined as the projection of the line connecting the origin with the true north pole on the just mentioned plane, whereas the x-axis is pointing, orthogonal to the y-axis, in eastern direction, being always on the tangent plane. We assume that the third axis is pointing upwards away from the ellipsoid center, orthogonal to both the x and y-axis, so to be normal to the x-y plane. In this case the navigation frame is called East-North-Up (ENU) frame. If one swaps the x and y-axis and inverts the direction of the z-axis, one comes to defined the North-East-Down (NED) frame, that is also frequently used in navigation. We preferred to adopt the latter convention, namely the NED one. This frame is very useful for attitude determination because it remains fixed with the moving object but keeps its axes orientated to the North and East direction, so that one can easily recover the orientation of the vehicle with respect, for example, to the North direction.

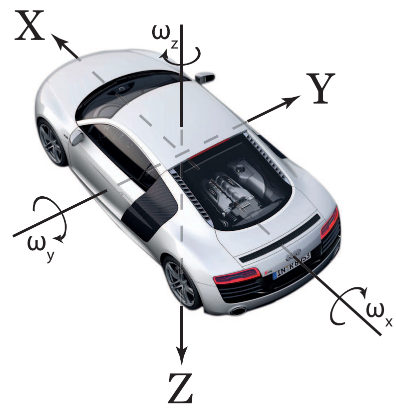

Figure 2.2: Illustration of the body-fixed coordinate frame and main rotation axes

2.1.3 Body-fixed coordinate frame

The body coordinate frame (Figure 2.2), called simply body frame, is usually centered in a specific point of object for which one wants to estimate its position. Its origin is so coincident to those of the navigation frame, but its orientation remains fixed with the moving object. Usually, the three axes are aligned so that the x-axis is oriented along the main movement direction of the vehicle, so to point in the "forward" direction, the y-axis is orthogonal to the x-axis pointing "right" and the z-axis is pointing "down", being orthogonal to both the x and the y-axis. Usually, the plane spanned by the x and y-axis is aligned so to match the horizontal section of the vehicle. These axes often take the name of roll (x-axis), pitch (y-axis) and yaw or heading axis (z-axis), and they are also the axes on which the inertial sensors are aligned to.

2.2 Coordinate frame transformations

2.2.1 Attitude parametrization using Euler angles

There exist several ways to transform a vector's coordinates from one coordinate frame to another. In our solution, we rely on the Euler angles rotation matrices, which rotate the vector consequently around each coordinate axes by angles that are named Euler angles. In this transformation, neither scaling nor transposition are taken into account, but only rotations are involved.

The Euler rotations are a predefined sequence of three rotations in a three dimensional, Cartesian space. It is performed by successive application of the three rotation matrices about specific axes. The rotation matrices are defined as follows:

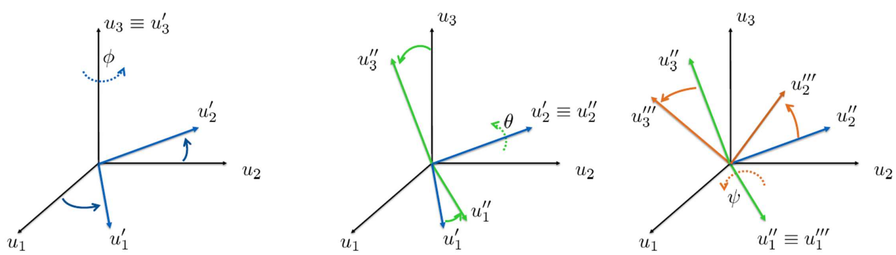

Figure 2.3: Successive rotations about ϕ, θ and ψ respectively

$$R_1(\alpha) = \begin{bmatrix} 1 & 0 & 0 \\ 0 & \cos\alpha & \sin\alpha \\ 0 & -\sin\alpha & \cos\alpha \end{bmatrix}; \ R_2(\alpha) = \begin{bmatrix} \cos\alpha & 0 & -\sin\alpha \\ 0 & 1 & 0 \\ \sin\alpha & 0 & \cos\alpha \end{bmatrix}; \qquad (2.1)$$

$$R_3(\alpha) = \begin{bmatrix} \cos\alpha & \sin\alpha & 0 \\ -\sin\alpha & \cos\alpha & 0 \\ 0 & 0 & 1 \end{bmatrix}$$

where $R_j(\alpha)$ represents the rotation about the j-th axis by the angle α. They are orthogonal matrices, so $R_j^{-1}(\alpha) = R_j^{\mathrm{T}}(\alpha) = R_j(-\alpha)$. It is important to denote that the specific order of the rotations has to be taken into account, because the rotation operations are not commutative: $R_1(\alpha)R_2(\beta) \neq R_2(\beta)R_1(\alpha)$. This property can be clarified when considering the transformation of a vector, say $\vec{x}$, from a certain t-frame to another s-frame:

$$\vec{x}^{\,s} = R_3(\psi)R_2(\theta)R_1(\varphi)\vec{x}^{\,t}$$

The vector $\vec{x}^t$ is first rotated around the (common) 1-axis, then rotated around the (new!) 2-axis, and finally rotated around the (even newer!) 3-axis. The successive rotation process is shown graphically in Figure 2.3. [3]

2.2.2 Transformation from the navigation frame to the earth-centered earth-fixed frame

The transformation from the navigation frame to the earth-centered earth-fixed frame (ECEF) is complicated by the fact that the two frames do not share the same origin. For most of the applications, however, this is not an issue as one is only interested on the relative orientation of the respective axes. The rotation matrix that describes the transformation from the navigation to the ECEF frame can be derived using Euler angles. First, rotate about the East-axis (y-axis) of the North-East-Down navigation frame (NED) by the positive angle (right hand rule) $\phi + \frac{\pi}{2}$, then rotate about the (new) Down axis (z-axis) by the negative angle $-\lambda$:

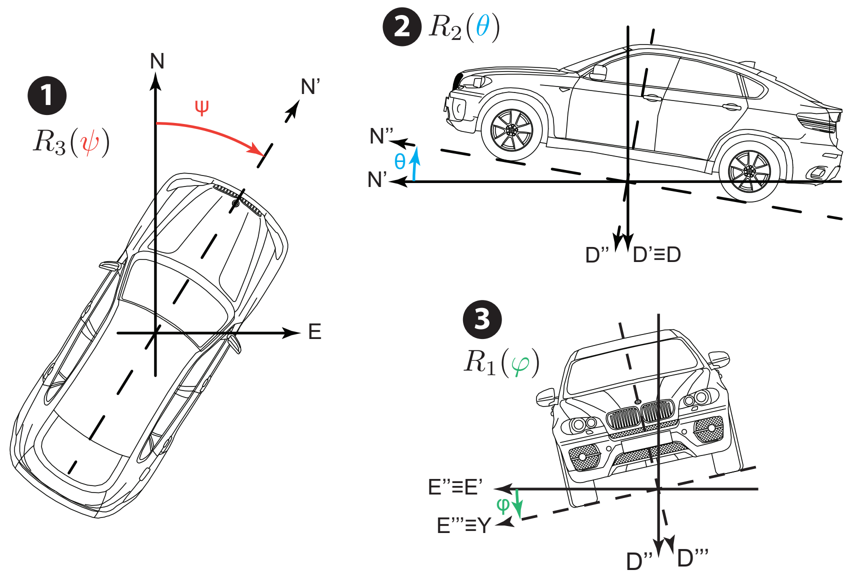

Figure 2.4: Graphical representation of the three successive rotations that involve the navigation-to-body frame coordinate transformation

$$R_n^e = R_3(-\lambda)R_2(\phi + \frac{\pi}{2}) \tag{2.2}$$

where with (ϕ, λ) it is meant respectively the latitude and longitude in radians of the origin of the considered navigation frame w.r.t. the earth-centered earth-fixed frame.[2]

The rotation matrix becomes the notation R_s^t, where the subscript s is the origin coordinate frame and the superscript t is the destination coordinate frame for the rotation. In other words, R_s^t describes the rotation from the s-frame to the t-frame. Due to the fact that R_n^e is a product of orthogonal matrices and thus orthogonal itself, the inverse transform from the ECEF to the navigation frame can be performed simply as:

$$R_e^n = (R_n^e)^{-1} = R_2(-\phi - \frac{\pi}{2})R_3(\lambda)$$

2.2.3 Transformation from the body frame to the navigation frame

The transformation from the body-fixed frame into the navigation frame can be performed as usual by using the Euler attitude angles. In this case, the angles are the bank (denoted by φ), elevation (denoted by θ), and heading (denoted by ψ) angles. In our model, the heading angle is defined as the angle between the North-axis of the NED navigation frame and the projection of the roll-axis or x-axis of the body frame into the North-East plane of the NED frame, whereas the elevation angle is defined as the angle between the roll-axis or x-axis of the body frame and its projection on the North-East plane of the NED frame.

By applying successive rotations and using Euler rotation matrices, to rotate from the body to the navigation frame one has to first apply a rotation around the x-axis by the negative angle $-\varphi$, then apply a rotation about the new y-axis by the negative angle $-\theta$, finally apply a third rotation around the even newer z-axis by a negative angle of $-\psi$:

$$R_b^n = R_3(-\psi)R_2(-\theta)R_1(-\varphi) \tag{2.3}$$

Again, using the orthogonality property of the rotation matrix one can define the inverse rotation as:

$$R_n^b = (R_b^n)^{-1} = R_1(\varphi)R_2(\theta)R_3(\psi)$$

The latter rotation definition is also represented in Figure 2.4.

2.3 Time derivative of rotating quantities

The angular rate or angular velocity is the time derivative of an angle, in other words it describes the "speed" of a rotation around a specific axis. When a coordinate frame is rotating w.r.t. another coordinate frame, the formula that describes how to properly transform a time derivative of a vector from one frame into another is the so-called law of Coriolis:

$$\begin{aligned} R_s^t \dot{\vec{x}}^{\,s} &= \dot{\vec{x}}^{\,t} + \vec{\omega}_{st}^{\,t} \times \vec{x}^{\,t} \\ &= \dot{\vec{x}}^{\,t} + \Omega_{st}^{\,t} \vec{x}^{\,t} \end{aligned} \tag{2.4}$$

where with $\vec{\omega}_{st}^{\,t}$ it is meant the angular velocity vector of the t-frame (second subscript) w.r.t. the s-frame (first subscript) with coordinates that are given in the t-frame (superscript). It describes around which axes the t-frame rotates w.r.t. the s-frame. The second term on the right-hand side of equation 2.4 is the additional displacement $\dot{\vec{x}}$ is subject to because of the infinitesimal rotation of the frame. It is to be noted that this term, for definition of the vector product, is normal to the plane spanned both by the angular velocity vector $\vec{\omega}_{st}^{\,t}$ and the vector $\vec{x}^{\,t}$, thus pointing in the direction of the rotation as "seen" by the t-frame. The term $[\vec{\omega}_{st}^{\,t}\times]$ can be rewritten using the skew-symmetric representation of vector $\vec{\omega}_{st}^{\,t}$, namely $\Omega_{st}^{\,t}$, which is a skew-symmetric matrix defined by:

$$\Omega = \begin{bmatrix} 0 & -\omega_3 & \omega_2 \\ \omega_3 & 0 & -\omega_1 \\ -\omega_2 & \omega_1 & 0 \end{bmatrix}$$

where $\vec{\omega} = [\omega_1, \omega_2, \omega_3]^{\mathrm{T}}$ is the angular velocity vector.

Another way to express the Coriolis Law is with the following relationship:

$$\dot{R}_s^t = \Omega_{ts}^t R_s^t \tag{2.5}$$

which can be easily derived from equation 2.4 and points out that the time differential of rotation matrix $\dot{R}_s^t$ is completely defined by the skew-symmetric matrix Ω_{st}^t that contains the information on the relative rotation velocity between the two coordinate frames[1].

2.4 Transformation of the sensed angular rates into the Euler attitude angles

The angular rate values sensed by the three gyroscopes can be expressed as an angular velocity vector. As the gyroscopes are inertial sensors, they sense any angular displacement that potentially can modify their inertia, say, even the one caused by the orbiting of the earth around the sun. The correct definition of their angular velocity vector should be done w.r.t an inertial frame, such as a frame that obeys the well-known Isaac Newton's laws of motion, in which a body at rest stays at rest in the absence of applied forces. Thus, the angular velocity vector of the sensed angular rates by the gyroscopes can be written as:

$$\vec{\omega}_{ib}^{\,b} = \vec{\omega}_{ie}^{\,b} + \vec{\omega}_{en}^{\,b} + \vec{\omega}_{nb}^{\,b} \tag{2.6}$$

thus decomposing it as the sum of three angular velocity vectors. In equation 2.6, the suffixes i, e, n and b stands for the inertial, ECEF, navigation and body frame respectively. The first decomposition term includes the angular velocity due to both the orbiting of the earth and the earth rotation itself, whereas the second includes the rotations caused by the reorientation of the north, east and down directions of the navigation frame as the vehicle travels along the earth's surface, whereas the third one describes the actual rotation between the navigation and the body frame, which includes the quasi-totality of the rotational dynamics.

Moreover, the angular velocity vector $\vec{\omega}_{nb}^{\,b}$ in equation 2.6 can be expressed, using the Euler angles representation, as the sum of three vectors each representing the successive rotation around one specific axis:

$$\begin{aligned}\vec{\omega}_{nb}^{\,b} &= \vec{\omega}_{nb_2}^{\,b} + \vec{\omega}_{b_2b_1}^{\,b} + \vec{\omega}_{b_1b}^{\,b} \\ &= R_{b_1}^b R_{b_2}^{b_1} \vec{\omega}_{nb_2}^{\,b_2} + R_{b_1}^b \vec{\omega}_{b_2b_1}^{\,b_1} + \vec{\omega}_{b_1b}^{\,b}\end{aligned} \tag{2.7}$$

where the coordinate frames b_1 and b_2 are the intermediate coordinate frames that are considered when applying successive rotations. The three expressions of the angular rotation vectors on the second equality of equation 2.7 describe the actual angular rates that are sensed when being fixed w.r.t. one of the intermediate coordinate frames. The rotation matrices $R_{b_1}^b$ and $R_{b_2}^{b_1}$ describe a rotation from one intermediate coordinate frame to another, thus representing

R_1 and R_2, respectively, as defined in section 2.2.1. In this configuration, only one component of the respective angular velocity vector is unequal to zero, as the rotations are always performed around one of the canonical axes of the intermediate coordinate frames:

$$\vec{\omega}_{b_1 b}^{\,b} = \begin{bmatrix} \dot{\varphi} \\ 0 \\ 0 \end{bmatrix};\ \vec{\omega}_{b_2 b_1}^{\,b_1} = \begin{bmatrix} 0 \\ \dot{\theta} \\ 0 \end{bmatrix};\ \vec{\omega}_{n b_2}^{\,b_2} = \begin{bmatrix} 0 \\ 0 \\ \dot{\psi} \end{bmatrix} \tag{2.8}$$

The angular rates ($\dot{\varphi}$, $\dot{\theta}$, $\dot{\psi}$) in equation 2.8 are nothing else but the time derivative of the Euler angles defined in section 2.2.1. The solution of equation 2.7 for (φ, θ, ψ) involves so the solution of the following differential equation:

$$\begin{bmatrix} \dot{\varphi} \\ \dot{\theta} \\ \dot{\psi} \end{bmatrix} = R_{\text{Euler}} \vec{\omega}_{nb}^{\,b} \tag{2.9}$$

where

$$R_{\text{Euler}} = \begin{bmatrix} 1 & \sin(\varphi)\tan(\theta) & \cos(\varphi)\tan(\theta) \\ 0 & \cos(\varphi) & -\sin(\varphi) \\ 0 & \sin(\varphi)\sec(\theta) & \cos(\varphi)\sec(\theta) \end{bmatrix} \tag{2.10}$$

is the so-defined Euler matrix which describes the nonlinear relationship between $\vec{\omega}_{nb}^{\,b}$ and the time derivative of the Euler attitude angles. Integrating differential equation 2.9 would result in finding the desired attitude angles[1].

2.5 Relative motion kinematics

If one has to describe the relative motion between two coordinate frames in which one is not an inertial frame, that is a frame that does modify Newton's inertia during its observation, then one has to take particular attention when time differentiating the position equations. A vector that describes the position of a point particle w.r.t. an inertial frame can be written as:

$$\vec{r}^{\,i} = R_b^i \vec{r}^{\,b} \tag{2.11}$$

where $\vec{r}^{\,b}$ is the position vector describing the same point but w.r.t another coordinate frame, say, the body-fixed frame. Differentiating yields

$$\begin{aligned} \dot{\vec{r}}^{\,i} &= \dot{R}_b^i \vec{r}^{\,b} + R_b^i \dot{\vec{r}}^{\,b} && (2.12) \\ &= \Omega_{ib}^i R_b^i \vec{r}^{\,b} + R_b^i \dot{\vec{r}}^{\,b} \\ &= R_b^i \left(\dot{\vec{r}}^{\,b} + \Omega_{ib}^b \vec{r}^{\,b} \right) && (2.13) \end{aligned}$$

where the second expression of equation 2.12 has been obtained by applying the expression of Coriolis law of equation 2.5 and the third one with the relation $\Omega_{ib}^i R_b^i = R_b^i \Omega_{ib}^b$. Differentiating again yields

$$\ddot{\vec{r}}^i = \dot{R}_b^i \dot{\vec{r}}^b + \dot{R}_b^i \Omega_{ib}^b \vec{r}^b + R_b^i \ddot{\vec{r}}^b + R_b^i \dot{\Omega}_{ib}^b \vec{r}^b + R_b^i \Omega_{ib}^b \dot{\vec{r}}^b \tag{2.14}$$

substituting again $\dot{R}_b^i$ as in equation 2.5 and rearranging terms yields

$$\ddot{\vec{r}}^i = R_b^i \left(\ddot{\vec{r}}^b + 2\Omega_{ib}^b \dot{\vec{r}}^b + \dot{\Omega}_{ib}^b \vec{r}^b + \Omega_{ib}^b \Omega_{ib}^b \vec{r}^b \right) \tag{2.15}$$

where

$\ddot{\vec{r}}^b$	is the acceleration of the point particle in the body-fixed frame
$2\Omega_{ib}^b \dot{\vec{r}}^b$	is the Coriolis acceleration
$\dot{\Omega}_{ib}^b \vec{r}^b$	is the tangential acceleration
$\Omega_{ib}^b \Omega_{ib}^b \vec{r}^b$	is the centripetal acceleration

Equation 2.15 describes the acceleration of a point particle expressed into a non-inertial coordinate frame, as for example here the body-fixed frame.[2]

Chapter 3

The Inertial Navigation System

The Inertial Navigation System (INS) is a form of Dead Reckoning (DR) navigation system that doesn't rely on external reference, but works "on it's own", therefore is called an autonomous system. It is able to provide information about position, velocity and attitude from measurements taken from an inertial sensor and based on DR principles. Given specific initial conditions, the system is able to provide the vehicle's attitude by integrating the angular rate measurements once and their absolute position by double integration of the acceleration measurements.[2]

3.1 The inertial measurement unit (IMU)

The inertial measurement unit (IMU) consists of a set of three accelerometers, arranged on three orthogonal axes, and a set of three gyroscopes, also aligned with the same reference axes. The platform on which the sensors are mounted can be stabilized by a set of gimbals and servo motors (so-called gimbalized or stabilized mechanization), which is often very expensive but also very accurate, or firmly attached on the vehicle (so-called strapdown mechanization), which is much less expensive, very robust but less accurate.

The main drawback of such a navigation system is the presence of unpredictable and variable offset errors in their measurements, the so-called measurement biases. The main focus on research is based on finding an appropriate model for such errors, so to be able to estimate and correct for them.

The fundamental difference between gimbalized and strapdown IMUs is on the significance of the biases: the former is able to substantially reduce the errors thanks to the gimbalized structure that permits the platform to remain aligned with the local North, East and Down coordinate frame; whereas the latter, whose is firmly attached onto the mounting platform, suffers from all dynamics and vibrations from the object where it is mounted on. We preferred the second approach mainly for economical reasons, but also because of the increased robustness and nearly unnecessary maintenance.[1]

3.1.1 Movement model

IMU-based positioning relies simply on the integration of inertial sensed accelerations, and thus mathematically involves the solution of a differential equation, which in practice is solved by numerical integration. The differential equation is the following so-called navigation equation:

$$\ddot{\vec{x}} = \vec{g}(\vec{x}) + \vec{a} \tag{3.1}$$

where $\vec{x}$ is the position vector, $\vec{g}(\vec{x})$ the gravity acceleration vector, which in general is position-dependent, and $\vec{a}$ the superposition of all external accelerations that are sensed by the accelerometers. This navigation equation should be then expressed in the local frame defined by the orientation of the accelerometers w.r.t. the platform on which they are mounted on, and then transformed to the right navigation frame in order to be able to extrapolate the absolute position and attitude of the vehicle in the desired frame.

The numerical integration is performed after a linear approximation of the differential equation and, as the integration time is very short (about 0.01 seconds), this approach should be sufficiently accurate for our purposes. For the absolute position determination, this can be modeled simply by the following equations:

$$\begin{aligned}
\vec{x}_{n+1} &= \vec{x}_n + \Delta t \cdot \vec{v}_n + \frac{\Delta t^2}{2}\vec{a}_n + \eta_{x,\,n+1} && (3.2)\\
\vec{v}_{n+1} &= \vec{v}_n + \Delta t \cdot \vec{a}_n + \eta_{v,\,n+1} && (3.3)\\
\vec{a}_{n+1} &= \vec{a}_n + \eta_{a,\,n+1} && (3.4)
\end{aligned}$$

where n is the sample index, Δt the integration time, and $\vec{v} = \dot{\vec{x}}$, $\dot{\vec{v}} = \vec{a}$. All terms are subject to white Gaussian noise, which is represented by η.

Following the same approach for the attitude determination, the Euler attitude angles (heading, elevation and bank) can be obtained by:

$$\begin{aligned}
\psi_{n+1} &= \psi_n + \Delta t \cdot \dot{\psi}_n + \eta_{\psi,\,n+1} && (3.5)\\
\theta_{n+1} &= \theta_n + \Delta t \cdot \dot{\theta}_k + \eta_{\theta,\,n+1} && (3.6)\\
\varphi_{n+1} &= \varphi_n + \Delta t \cdot \dot{\varphi}_n + \eta_{\rho,\,n+1} && (3.7)
\end{aligned}$$

where ψ, θ, ϕ are respectively the heading, bank and elevation angles, whereas $\dot{\psi}, \dot{\theta}, \dot{\phi}$ represent their time derivatives, namely the heading, elevation and bank rate. It has to be noted that the latter do not represent the values sensed by the gyroscopes in our model, but are derivative of Euler angles. The Euler angles represents respectively the three successive rotations that describe the orientation of the vehicle w.r.t. a specific coordinate frame, as pointed out in section 2.4. The η term stands, as before, for Gaussian noise.

3.1.2 Measurement model

The measurements performed by the IMU includes both the acceleration measurements performed by the accelerometers and the angular rate measurements performed by the gyroscopes. As mentioned before, the inertial measurement units suffer mainly from bias errors, which unfortunately sum up when performing numerical integration. For this reason, it is necessary to model this drift by adding a certain measurement bias to the true value, which then should be estimated with the help of GPS-based measurements, that are known to be bias-free. In addition, for the acceleration vector estimation, it should be noted that the accelerometers sense both the external accelerations withstood by the vehicle and the acceleration due to the gravity field. For this reason, it is necessary to subtract the gravity vector from the acceleration measurement.

The acceleration measurements are modeled as:

$$\vec{f} = \vec{a} - \vec{g}(\vec{x}) + \vec{b}_a + \eta_{\tilde{a}} \tag{3.8}$$

in which $\vec{f}$ represents the measured accelerations (also called specific force vector) and $\vec{b}_a$ the acceleration bias vector, given respectively in the three body-frame axes. $\eta_{\tilde{a}}$ is modeled as Gaussian noise. The gravity vector is projected along the body-frame axes as:

$$\vec{g}(\vec{x}) = g(\vec{x}) \cdot \begin{bmatrix} -\sin(\theta(\vec{x})) \\ \cos(\theta(\vec{x}))\sin(\varphi(\vec{x})) \\ \cos(\theta(\vec{x}))\cos(\varphi(\vec{x})) \end{bmatrix} \tag{3.9}$$

in which $g(\vec{x})$ is the absolute position dependent local gravity acceleration magnitude that is projected into the three components of the body coordinate frame using the value of the elevation and bank angles.

The measurements coming from the gyroscopes measure the angular rates around the three axes of the frame on which they are mounted on, and can be modeled as:

$$\tilde{\vec{\omega}}_{ib}^{b} = \begin{bmatrix} \tilde{\omega}_X \\ \tilde{\omega}_Y \\ \tilde{\omega}_Z \end{bmatrix} = \begin{bmatrix} \omega_X + b_{\omega_X} + \eta_{\omega_X} \\ \omega_X + b_{\omega_X} + \eta_{\omega_X} \\ \omega_X + b_{\omega_X} + \eta_{\omega_X} \end{bmatrix} \tag{3.10}$$

where the values with a tilde ($\tilde{}$) represent the measured quantities, b stands for the bias error and η is modeled as Gaussian noise.

As said in section 2.4, the just mentioned angular rate vector can be split in several angular rates

$$\begin{aligned} \vec{\omega}_{ib}^{\,b} &= \vec{\omega}_{ie}^{\,b} + \vec{\omega}_{en}^{\,b} + \vec{\omega}_{nb}^{\,b} \\ &= \vec{\omega}_{ie}^{\,b} + \vec{\omega}_{en}^{\,b} + (R_{\text{Euler}})^{-1} \begin{bmatrix} \dot{\varphi} \\ \dot{\theta} \\ \dot{\psi} \end{bmatrix} \end{aligned}$$

where in the second expression of the above equation, the relationship of equation 2.9 has been used.

3.2 INS Mechanization

The process of INS Mechanization consists of converting the sensor's input into useful navigation parameters, e.g. into the position, velocity and attitude information of the moving object, given into a specific coordinate frame. The mechanization process starts with specific initial values as input and proceeds iterating over the sensor's output samples.

3.2.1 INS Mechanization in the Earth-centered Earth-fixed frame

In our sensor fusion model, we chose to perform INS mechanization into the Earth-centered Earth-fixed (ECEF) frame, because our estimated parameters in our Kalman-Filter approach (see section 5.2.1) are given in this coordinate frame.

The output of an accelerometer, called also specific force vector, can be modeled as:

$$\vec{f}^{\,i} = \vec{a}^{\,i} - \vec{g}^{\,i} \tag{3.11}$$

where $\vec{a}^i$ is the acceleration of the body, and $\vec{g}^{\,i}$ is called the gravitational vector, which models the gravitational field of the body positioned in $\vec{r}^{\,i}$ w.r.t. an inertial frame. All coordinates are given in the inertial frame i.

By substituting $\vec{a}^{\,i}$ with the expression of $\ddot{\vec{r}}^i$ from equation 2.15 and by applying a rotation R_i^e from the inertial to the ECEF frame, we obtain

$$\vec{f}^{\,i} + \vec{g}^{\,i} = R_e^i \left(\ddot{\vec{r}}^{\,e} + 2\Omega_{ie}^e \dot{\vec{r}}^{\,e} + \dot{\Omega}_{ie}^e \vec{r}^{\,e} + \Omega_{ie}^e \Omega_{ie}^e \vec{r}^{\,e} \right) \tag{3.12}$$

where, without loss of generality, we have simply substituted the index of the target coordinate frame from b to e, as we mean now the ECEF frame.

Now, as the earth rotation rate is approximately constant, we can assume that $\dot{\Omega}_{ie}^e = \mathbf{0}$. Moreover, the gravitational field in the ECEF frame can be expressed as

$$R_i^e \vec{g}^{\,i} = \vec{g}^e + \Omega_{ie}^e \Omega_{ie}^e \vec{r}^e$$

as the gravitational vector $\vec{g}^{\,i}$, once rotated into the ECEF frame, is subject to the earth rotation.

By taking into account what has been just pointed out, equation 3.12 can be rewritten as:

$$\vec{f}^{\,i} = R_e^i \left(\ddot{\vec{r}}^{\,e} + 2\Omega_{ie}^e \dot{\vec{r}}^{\,e} - \vec{g}^{\,e} \right) \tag{3.13}$$

Solving for $\ddot{\vec{r}}^{\,e}$ yields:

$$\ddot{\vec{r}}^{\,e} = R_b^e \vec{f}^{\,b} - 2\Omega_{ie}^{\,e} \dot{\vec{r}}^{\,e} + \vec{g}^{\,e} \tag{3.14}$$

which is the expression of the acceleration of the body with coordinates given in the ECEF frame.

Furthermore, the Coriolis law from equation 2.5, can be rewritten for the ECEF frame as

$$\dot{R}_b^e = R_b^e \Omega_{eb}^{\,b} \tag{3.15}$$

By noting that $\Omega_{ib}^{\,b} = \Omega_{ie}^{\,b} + \Omega_{eb}^{\,b}$ the above equation can be rewritten as

$$\dot{R}_b^e = R_b^e \left(\Omega_{ib}^{\,b} - \Omega_{ie}^{\,b}\right) \tag{3.16}$$

which gives us an expression of the body's angular rate in the desired ECEF frame. [2]

Chapter 4

The Global Positioning System

The Global Positioning System (GPS) is the most common and powerful outdoor navigation system. Developed by the US Department of Defense (DoD) in the 1970s, it was once thought for military purposes. It became fully operational in 1995, but until 2000 the signal for civil use was artificially degraded so that only the military could benefit of the maximum performance. Until now, many enhancements have been developed to improve position accuracy: new signals have been developed with improved accuracy and many satellite-based and ground-based augmentation systems (SBAS and GBAS, respectively) have been developed to provide the user with correction data to reduce atmospheric, orbital and satellite clock errors and to enhance the system's integrity.

But GPS isn't the only operative Global Navigation Satellite System (GNSS). At time of writing, many more of these systems are being developed: The Russian Global Navigation System (GLONASS), developed by the Russian Aerospace Defense Forces, is the main alternative to GPS. Being developed since the late 1980s, it has reached global coverage in 2011, but since then is still under development. Recently, more and more commercial GNSS receivers are including the capability of decoding GLONASS signals, too. Moreover, the European Space Agency (ESA), together with the European Union (EU) has been developing its own GNSS project called Galileo. Unlike GPS and GLONASS, Galileo has been developed with the aim to provide a high-precision signal that will enable a very reliable integer Ambiguity Resolution (AR), providing the user with a centimeter-level accuracy. Unfortunately, Galileo satellite constellation is still incomplete, the total constellation of 24 satellites will be reached only in 2020 [4].

The growing number of GNSS systems will provide a much better measurement availability, more robustness, and could finally enable reliable integer Ambiguity Resolution (AR) to substantially improve accuracy of RTK and PPP solutions.[5, 6]

4.1 Measurement models

In the following, the models for the GPS pseudorange, carrier phase and Doppler measurements shall be outlined. We note that in our implementation, we strongly rely on GPS carrier phase measurement for maximizing positioning accuracy possibly up to centimeter level. This requires correct resolution of the integer ambiguities, topic that will be briefly discussed in section 4.4. Although this has been developed using only signals coming from GPS satellites, the extension of the subsequent model on Galileo or GLONASS measurements is theoretically immediate, because the latter GNSS systems rely on equivalent measurement models.

In the following, basic knowledge of GNSS measurements is required. This topic is treated exhaustively in [5] and in [7].

4.1.1 The pseudorange measurement

For the GPS pseudorange measurement, the following model is assumed:

$$\rho_r^k = \left(\vec{e}_r^{\,k}\right)^{\mathrm{T}} \left(\vec{r}_r - \vec{r}^{\,k}\right) + c(\delta_r - \delta^k) + I_r^k + T_r^k + \triangle\rho_{\mathrm{MP}}{}_r^k + \eta_r^k \tag{4.1}$$

where, apart from navigation parameters described in Appendix A.3, with $\triangle\rho_{\mathrm{MP}}{}_r^k$ it is meant the code phase multipath error.

4.1.2 The carrier phase measurement

For the GPS carrier phase measurement, the following model is assumed:

$$\lambda\phi_r^k = \left(\vec{e}_r^{\,k}\right)^{\mathrm{T}} \left(\vec{r}_r - \vec{r}^{\,k}\right) + c(\delta_r - \delta^k) - I_r^k + T_r^k + \lambda N_r^k + \triangle\varphi_{\mathrm{MP}}{}_r^k + \beta_r + \beta^k + \epsilon_r^k \tag{4.2}$$

where, apart from navigation parameters described in Appendix A.3, with $\triangle\phi_{\mathrm{MP}}{}_r^k$ it is meant the carrier phase multipath error, whereas the receiver and satellite biases are denoted by β_r and β^k, respectively.

4.1.3 The Doppler frequency measurement

For the GPS Doppler frequency measurement, the following model is assumed:

$$\begin{aligned} f_d &= f_R - f_T \\ &= -\frac{f_T}{c}\left((\vec{e}_r^{\,k})^{\mathrm{T}}(\vec{v}_r - \vec{v}^{\,k}) + c(\dot{\delta}_r - \dot{\delta}^k) - \dot{I}_r^k + \dot{T}_r^k + \frac{\partial}{\partial t}\triangle\phi_{\mathrm{MP}}{}_r^k + \eta_{d_r^k} \right) \end{aligned} \tag{4.3}$$

where f_R and f_T are the frequencies of the received and transmitted carrier signal, respectively, $\vec{v}_r$ and $\vec{v}^{\,k}$ describe the user and satellite velocity vector, whereas $\dot{\delta}^k$ and $\dot{\delta}_r$ represent the time derivative of the satellite and user clock errors. The time variability of the other error terms is smaller than the measurement noise, and so the quantities $\dot{I}_r^k$, $\dot{T}_r^k$ and $\frac{\partial}{\partial t}\triangle\rho_{\mathrm{MP}}{}_r^k$ can be neglected. The noise term $\eta_{d_r^k}$ is modeled as Gaussian noise.

4.2 Single and double differences

The main advantage in taking differences between measurements is to eliminate common sources of error. Taking equations 4.1 and 4.2 as reference, the single, satellite-to-satellite difference of both the code and the carrier phase can be modeled as:

$$\begin{aligned}
\rho_r^{kl} &= \rho_r^k - \rho_r^l \\
&= (\vec{e}_r^{\,k} - \vec{e}_r^{\,l})^T \cdot \vec{r}_r - (\vec{e}_r^{\,k})^T \cdot \vec{r}^{\,k} + (\vec{e}_r^{\,l})^T \cdot \vec{r}^{\,l} \ \ldots \\
&\quad -c(\delta^k - \delta^l) + I_r^{kl} + T_r^{kl} + \triangle\rho_{\mathrm{MP}}{}_r^{kl} + \eta_r^{kl}
\end{aligned} \tag{4.4}$$

$$\begin{aligned}
\lambda\phi_r^{kl} &= \lambda(\phi_r^k - \phi_r^l) \\
&= (\vec{e}_r^{\,kl})^T \cdot \vec{r}_r - (\vec{e}_r^{\,k})^T \cdot \vec{r}^{\,k} + (\vec{e}_r^{\,l})^T \cdot \vec{r}^{\,l} - c(\delta^k - \delta^l) \ \ldots \\
&\quad -I_r^{kl} + T_r^{kl} + \lambda N_r^{kl} + \triangle\varphi_{\mathrm{MP}}{}_r^{kl} + \beta^{kl} + \epsilon_r^{kl}
\end{aligned} \tag{4.5}$$

The latter satellite index l is referred the reference satellite, mostly chosen to be the one with the highest elevation angle. In this case, the common receiver clock error $c\delta_r$ and the common receiver bias β_r in the carrier phase equation cancel out.

This single differences can be also calculated on a second receiver and used to build up double differences, this is done by taking the difference of single-difference measurements coming from two different receivers and having the same satellite indexes kl. It can be modeled as:

$$\begin{aligned}
\rho_{12}^{kl} &= \rho_1^{kl} - \rho_2^{kl} \\
&= (\vec{e}_1^{\,kl})^T \cdot \vec{r}_1 - (\vec{e}_2^{\,kl})^T \cdot \vec{r}_2 - (\vec{e}_1^{\,k} - \vec{e}_2^{\,k})^T \cdot \vec{r}^{\,k} \ \ldots \\
&\quad +(\vec{e}_1^{\,l} - \vec{e}_2^{\,l})^T \cdot \vec{r}^{\,l} + I_{12}^{kl} + T_{12}^{kl} + \triangle\rho_{\mathrm{MP}}{}_{12}^{kl} + \eta_{12}^{kl}
\end{aligned} \tag{4.6}$$

$$\begin{aligned}
\lambda\phi_{12}^{kl} &= \lambda(\phi_1^{kl} - \phi_2^{kl}) = \\
&= (\vec{e}_1^{\,kl})^T \cdot \vec{r}_1 - (\vec{e}_2^{\,kl})^T \cdot \vec{r}_2 - (\vec{e}_1^{\,k} - \vec{e}_2^{\,k})^T \cdot \vec{r}^{\,k} \ \ldots \\
&\quad +(\vec{e}_1^{\,l} - \vec{e}_2^{\,l})^T \cdot \vec{r}^{\,l} - I_{12}^{kl} + T_{12}^{kl} + \lambda N_{12}^{kl} + \triangle\phi_{\mathrm{MP}}{}_{12}^{kl} + \epsilon_{12}^{kl}
\end{aligned} \tag{4.7}$$

By taking these differences, the satellite clock errors are the same on both receiver 1 and 2 and thus cancel out. In addition, the residual atmospheric differential errors I_{12}^{kl} and T_{12}^{kl} are typically much smaller than the absolute delays, as long as the distance from the two receivers is not too large (up to a few kilometers) [5].

4.3 Clock synchronization corrections

The measurement model for double differences described in section 4.2 does not exploit the lack of synchronicity between different receivers. If using compatible receivers, the temporal synchronicity can be achieved using a common oscillator[8]. However, if using low-cost GNSS receivers, this has to be back-corrected in software in form of a synchronization correction term as:

$$\begin{aligned} c_{12}^{kl} \quad = \quad & -\left\{ \left[\vec{e}_2^{\,k}(t) \right]^T \left[\vec{r}_2(t) - \vec{r}^{\,k}(t) \right] - \left[\vec{e}_2^{\,l}(t) \right]^T \left[\vec{r}_2(t) - \vec{r}^{\,l}(t) \right] \right\}_{t=t_n+\delta t_2} \\ & + \left\{ \left[\vec{e}_1^{\,k}(t) \right]^T \left[\vec{r}_2(t) - \vec{r}^{\,k}(t) \right] - \left[\vec{e}_1^{\,l}(t) \right]^T \left[\vec{r}_2(t) - \vec{r}^{\,l}(t) \right] \right\}_{t=t_n+\delta t_1} \end{aligned} \tag{4.8}$$

in which the time dependency of the e-vectors and the range vectors has been exploited. The time t_n refers to the reference time, namely the GPS-time, whereas the time difference δt_r refers to the difference between the reference time and the time of measurement of the receiver r [9].

4.4 Integer ambiguity resolution

The accuracy of the position estimation can be improved by exploiting the integer nature of the whole cycles of the carrier phase measurement. Its correct estimation is one of the most discussed topics in Precise Point Positioning (PPP) and Real Time Kinematics (RTK) approaches.

Without entering into details, the core of the problem is to minimize the following quantity:

$$\underset{\xi \in \mathbb{R}^3,\, N \in \mathbb{Z}^K}{\arg\min} \; \| \Psi - H\xi - AN \|^2_{Q_\Psi^{-1}} \tag{4.9}$$

having with

$$\Psi = \begin{bmatrix} \rho_{12}^{1,K} & \dots & \rho_{12}^{K-1,K} \\ \lambda\phi_{12}^{1,K} & \dots & \lambda\phi_{12}^{K-1,K} \end{bmatrix}^{\mathrm{T}}$$

the pseudorange and carrier phase double differenced synchronized measurements; with

$$\xi = \vec{b}_{12}$$

the baseline vector; and with

$$H = \begin{bmatrix} 1 \\ 1 \end{bmatrix} \otimes \left[\vec{e}_1^{\,1,K}, \, \dots \, , \, \vec{e}_1^{\,1-K,K} \right]^{\mathrm{T}}$$

and

$$A = \lambda \begin{bmatrix} \mathbf{0}_{(K-1)\times(K-1)} \\ \mathbf{1}_{(K-1)\times(K-1)} \end{bmatrix}$$

the matrices describing the geometry for the unknown baseline vector ξ and integer ambiguity vector N, respectively. The minimization has to be performed with a metrics described by the inverse of the measurement covariance matrix Q_Ψ^{-1}.

The norm can be decomposed by applying the orthogonal projector on the space of H, namely $P_H^\perp$, to the minimization term in equation 4.9. A real-valued estimation of the integer ambiguities can then be performed by

$$\hat{N} = \underset{N\in\mathbb{R}^K}{\arg\min} \left\| P_H^\perp \left(\Psi - AN\right) \right\|^2_{Q_\Psi^{-1}} \tag{4.10}$$

and the float estimation can be used to select the "best" integer candidate as

$$\breve{N} = \underset{N\in\mathbb{Z}^K}{\arg\min} \left\| \hat{N} - N \right\|^2_{Q_N^{-1}} \tag{4.11}$$

having with

$$Q_N^{-1} = \left(P_H^\perp A\right)^{\mathrm{T}} Q_\Psi^{-1} P_H^\perp A$$

the inverse of the float ambiguities covariance matrix.

The optimal integer candidate vector $\breve{N}$ can be found by applying a decorrelation algorithm, the Least-Squares Ambiguity Decorrelation Adjustment (LAMBDA). This procedure aims on decorrelating the least-squares ambiguities $\breve{N}$ based on the metrics given by the covariance matrix Q_N and by exploiting the integer nature of the candidates. Without entering into details, the procedure aims to find the best linear transformation that both diagonalizes the metrics described by Q_N^{-1} in order to minimize the correlations induced by measurement differentiation and that avoids the distortion of the transformed space in order to preserve the integer nature of the candidates. The goal is to find an integer valued, grid-preserving transformation Z given by

$$\tilde{Q}_N = Z Q_N Z^{\mathrm{T}} \tag{4.12}$$

in which Z is integer valued and $\tilde{Q}_N$ is as diagonal as possible. Such type of diagonalization may be obtained from a Cholesky triangular decomposition in which the off-diagonal elements of the triangular matrices are forced to be integer valued. Once that $\tilde{Q}_N$ is found, and assuming that it is approximately diagonal, the minimization term in equation 4.11, once transformed according to equation 4.12, may be rewritten as

$$\left\| \hat{N} - \tilde{N} \right\|^2_{\tilde{Q}_N^{-1}} = \sum_{k=1}^{K} \frac{\left(\tilde{N}^k - \hat{N}^{k|1,\,\ldots,\,k-1}\right)^2}{\sigma^2_{\hat{N}^{k|1,\,\ldots,\,k-1}}} \tag{4.13}$$

in which $\tilde{N}^k$ is the k-th transformed integer ambiguity and $\hat{N}^{k|1,\,\dots,\,k-1}$ denotes the k-th transformed float ambiguity estimate given that the ambiguities $\tilde{N}^1, \dots \tilde{N}^{k-1}$ have been already fixed to an integer value. Minimizing the float ambiguity residuals in equation 4.13 equals to find integer candidates $\tilde{N}^k$ such that

$$\sum_{k=1}^{K} \frac{\left(\tilde{N}^k - \hat{N}^{k|1,\,\dots,\,k-1}\right)^2}{\sigma^2_{\hat{N}^{k|1,\,\dots,\,k-1}}} \leq \chi^2 \tag{4.14}$$

in which $\chi^2 \in \mathbb{R}$ is chosen according to the float solution. Isolating the k-th term from the summation in equation 4.14 yields:

$$\frac{\left(\tilde{N}^k - \hat{N}^{k|1,\,\dots,\,k-1}\right)^2}{\sigma^2_{\hat{N}^{k|1,\,\dots,\,k-1}}} \leq \chi^2 - \sum_{l=1,\,l\neq k}^{K} \frac{\left(\tilde{N}^l - \hat{N}^{l|1,\,\dots,\,l-1}\right)^2}{\sigma^2_{\hat{N}^{k|1,\,\dots,\,l-1}}} \tag{4.15}$$

The terms of the summation on the right hand side of equation 4.15 are all positive definite and this enables to rewrite the inequality as

$$\frac{\left(\tilde{N}^k - \hat{N}^{k|1,\,\dots,\,k-1}\right)^2}{\sigma^2_{\hat{N}^{k|1,\,\dots,\,k-1}}} \leq \chi^2 - \sum_{l=1}^{k-1} \frac{\left(\tilde{N}^l - \hat{N}^{l|1,\,\dots,\,l-1}\right)^2}{\sigma^2_{\hat{N}^{k|1,\,\dots,\,l-1}}} \tag{4.16}$$

without altering its validity. Equation 4.16 may suggest a tree-search based recursive algorithm that is initialized with possible integer candidates for $\tilde{N}^1$ and is repeated recursively for the other candidates based on the initial supposition of the first fixed candidate. By doing so, for every supposed k-th integer candidate $\tilde{N}^k$, an equivalent integer fixing algorithm with reduced number of candidates (namely $K - k - 1$) can be performed.

A more exhaustive treatment of this topic can be found in [10]. For more insight on LAMBDA we refer to [11].

Chapter 5

Sensor Fusion: The extended Kalman Filter

By observing the pros and cons of referenced positioning and dead reckoning respectively, it has been observed that they are complementary: while GNSS-based positioning has a good long term accuracy and its errors are bounded to a few meters, on the other hand it has a relatively bad short-time accuracy, is dependent on the environment and provides a low data output rate. For INS-based positioning instead, the picture is mainly the opposite: it has a good short-time accuracy, is totally independent from the environment, provides high data output rate but suffers of a bad long-time accuracy due to the intrinsic integration in the computation algorithm.

In the past years, since the mass market lowered the price of both INS and GNSS sensors, such an integration became more and more interesting also because of a feasible probability of being commercialized.

To cite only a few, C. Hide and T. Moore [12] came up in 2005 with a tightly coupled GPS/INS solution using a low-cost Crossbow MEMS IMU and a Novatel GPS receiver. They performed sensor fusion at measurement level with a standard Kalman Filter having 3D IMU angular rate and acceleration measurements and the GPS ground differential pseudorange (they used a Leica GPS static receiver as reference receiver) and Doppler measurements as input. In addition, they performed Kalman Filter smoothing in post-processing to reduce the standard deviation of the errors. The results showed that they were able to bound the errors up to a few meters even in deep urban conditions with poor satellite visibility. The KF smoothing enabled to further reduce the error peaks.

Y. Li and others [13] presented in 2006 another tightly coupled GPS/INS solution using low-cost sensors and antennas. For the sensor fusion algorithm, they implemented a Sigma-Point Kalman Filter (SPKF), which has the advantage to better model the nonlinearities of a standard Extended Kalman Filter (EKF) approach by taking into account not only the first but also the second moment in the linearization process. They used, as usual, IMU 3D angular rate and acceleration measurements as well as GPS satellite single-difference pseudorange and Doppler measurements. As for the results, they point out that the SPKF does not give noticeable better results than a standard EKF approach, possibly because the nonlinearities are not large enough to leverage the improved linear approximation of the SPKF.

To conclude our citations, J. Georgy and others [14] designed in 2010 a slightly different approach using a Reduced Inertial Sensor System (RISS) instead of a full-IMU approach. They proposed a GPS/INS sensor fusion using only the Z-axis gyroscope measurement, the X- and Y-axis accelerometer measurements and the GPS undifferentiated pseudorange and Doppler measurements driven by an enhanced Particle Filter (PF) called Mixture PF. In addition, they used the wheel sensor on the car to aid the filter with speed information, too. The main advantage of using RISS instead of full IMU relies, in their opinion, in being able to extract the elevation and bank attitude angles directly from the acceleration measurements by adopting a suitable gravitational model. This in turn avoids suffering from third order position errors that otherwise would be induced by the necessary integration of the gyroscope measurements. Results have been compared with a usual INS/GPS approach and have shown a better performance in term of position accuracy.

In the following, our model for a EKF INS/GPS tight coupling is presented. We shall note that, in contrast to the just outlined methods we strongly rely on carrier phase positioning and on measurement differentiation. This has the drawback that the integer ambiguities have to be correctly resolved, and this isn't a trivial task, but has the strong advantage of the substantially reduced noise level and multipath errors of the carrier phase measurements.

From now on, the reader is advised on basic Bayesian estimation and Kalman Filter knowledge, otherwise we propose [15] and [2] as references for this topic.

5.1 Sensor set-up

Figure 5.1 shows our set-up for the tightly coupled RTK position and attitude determination. The GNSS antennas 1 and 2 are firmly attached onto the car rooftop, whereas the third one is assumed as static and its position as known. The IMU is also mounted inside the car and its reference axes are aligned with the car longitudinal, lateral and vertical axes.

For every epoch, we estimate both the RTK and the attitude baseline, the former being defined as a function of the absolute positions $\vec{x}_1$ and $\vec{x}_3$:

$$\vec{b}_{13}\,(\vec{x}_1,\,\vec{x}_3) = \vec{x}_1 - \vec{x}_3$$

and the latter being defined as a function of Euler attitude angles:

$$\vec{b}_{12}\,(\psi,\,\theta) = \left\|\vec{b}_{12}\right\| \begin{bmatrix} \cos(\theta)\cos(\psi) \\ \cos(\theta)\sin(\psi) \\ -\sin(\theta) \end{bmatrix}$$

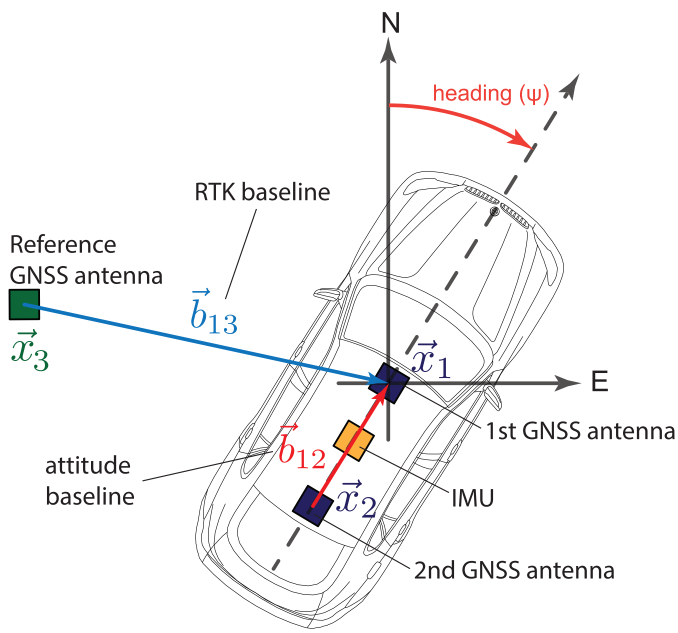

Figure 5.1: GNSS and inertial sensor set-up

It should be noted that the absolute position $\vec{x}_3$ of the reference GNSS antenna is static and known and the norm $\parallel \vec{b}_{12} \parallel$ of the attitude baseline is always constant and known a priori, too.

5.2 KF Modeling

In the following, the state-transition and measurement models of our KF approach shall be presented. Moreover, the parameters of the state and measurement vectors are outlined, and a more detailed model description for inertial and GNSS-based state parameters and measurements is presented.

5.2.1 State transition model

The state transition or state-space model describes how the states or parameters of the system vary with time based on a specific linear model.

In our KF modeling, the state parameter transition between subsequent epochs is given by:

$$x_n^- = \Phi_{n-1} x_{n-1}^+ + w_n \tag{5.1}$$

where x_{n-1}^+ represents the state vector, Φ_{n-1} the transition matrix of epoch $n-1$; x_n^- the predicted state vector of epoch n, and w_n the so-called process or

Parameter	Description
$\vec{b}_{13}$	Position of GNSS receiver 1 relative to GNSS receiver 3 [m]
$\vec{v}_1$	Velocity of GNSS receiver 1 [m/s]
$\vec{a}_1$	Acceleration of GNSS receiver 1 [m/s^2]
ψ	Heading angle of vehicle [rad]
$\dot{\psi}$	Heading angular rate of vehicle [rad/s]
θ	Elevation angle of vehicle [rad]
$\dot{\theta}$	Elevation angular rate of vehicle [rad/s]
φ	Bank angle of vehicle [rad]
$\dot{\varphi}$	Bank angular rate [rad/s]
$\lambda N_3^{\text{sd}} + I^{\text{sd}}$	Sum of SD integer amb. of GNSS rec. 3 and SD ionospheric delay [m]
$\triangle\rho_{\text{MP}1}^{\text{sd}}$	Single-difference code-phase multipath of GPS receiver 1 [m]
$\triangle\rho_{\text{MP}2}^{\text{sd}}$	Single-difference code-phase multipath of GPS receiver 2 [m]
$b_{\vec{\omega}}$	Bias vector of body-fixed frame angular rate measurement [rad/s]
$b_{\vec{a}}$	Bias vector of body-fixed frame acceleration measurements [m/s^2]

Table 5.1: Description of the components of the state vector x

system noise vector. Together with the process noise vector one can define the process noise covariance matrix as:

$$Q_n = \mathbf{E}\left[w_n w_n^{\mathrm{T}}\right] \tag{5.2}$$

This matrix has the variances of the state parameter's estimates based on the system model.

The estimated parameters are collected inside the state vector, that is given by:

$$x = \left[\vec{b}_{13}^{\mathrm{T}},\, \vec{v}_1^{\mathrm{T}},\, \vec{a}_1^{\mathrm{T}},\, \psi,\, \dot{\psi},\, \theta,\, \dot{\theta},\, \varphi,\, \dot{\varphi},\, \left(N_3^{\text{sd}} + I^{\text{sd}}\right)^{\mathrm{T}},\, \left(\triangle\rho_{\text{MP}1}^{\text{sd}}\right)^{\mathrm{T}},\, \left(\triangle\rho_{\text{MP}2}^{\text{sd}}\right)^{\mathrm{T}},\, b_{\vec{\omega}}^{\mathrm{T}},\, b_{\vec{a}}^{\mathrm{T}}\right]^{\mathrm{T}} \tag{5.3}$$

Table 5.1 explains the meaning of each component of the state vector.

Due to heterogeneous measurement nature, for each specific epoch only a subset of the state vector can be updated, and this depends mainly on the sensor type (GPS or IMU) which is providing the measurements in that specific epoch. To describe this selection, we denote as $s_n^x(\gamma_n, x_n)$ the subset of the state vector according to which sensor type γ_n provided the measurements at epoch n. The measurements coming from GPS sensors get a $\gamma_n = 1$, whereas measurements coming from the IMU sensor get a $\gamma_n = 2$. The corresponding subsets of the state vector are pointed out in the following equations:

$$
\begin{aligned}
s_n^x(1,\,x_n) &= \Big[\vec{b}_{13}^{\mathrm{T}},\,\vec{v}_1^{\,\mathrm{T}},\,\vec{a}_1^{\,\mathrm{T}},\,\psi,\,\dot{\psi},\,\theta,\,\dot{\theta},\,\left(N_3^{\mathrm{sd}}+I^{\mathrm{sd}}\right)^{\mathrm{T}},\,\ldots \\
&\qquad \left(\triangle\rho_{\mathrm{MP}}{}_1^{\mathrm{sd}}\right)^{\mathrm{T}},\,\left(\triangle\rho_{\mathrm{MP}}{}_2^{\mathrm{sd}}\right)^{\mathrm{T}},\,b_{\vec{\omega}}^{\mathrm{T}},\,b_{\vec{a}}^{\mathrm{T}}\Big]^{\mathrm{T}} \qquad (5.4) \\
s_n^x(2,\,x_n) &= \Big[\vec{b}_{13}^{\mathrm{T}},\,\vec{v}_1^{\,\mathrm{T}},\,\vec{a}_1^{\,\mathrm{T}},\,\psi,\,\dot{\psi},\,\theta,\,\dot{\theta},\,\varphi,\,\dot{\varphi},\,b_{\vec{\omega}}^{\mathrm{T}},\,b_{\vec{a}}^{\mathrm{T}}\Big]^{\mathrm{T}} \qquad (5.5)
\end{aligned}
$$

It should be also noted that in equation 5.4, from the vectors $N_3^{\mathrm{sd}} + I^{\mathrm{sd}}$ and $\triangle\rho_{\mathrm{MP}}{}_{1/2}^{\mathrm{sd}}$ only the components that refers to satellites that are visible and tracked in the specific epoch n are selected. It would have no sense to update the estimation for, let's say the single-difference integer ambiguity N_3^{kl} if the measurement coming from satellite k is not available in the considered epoch.

With reference to equation 5.1, the state transition model for selected subsets of state parameters are going to be described. In the following, the subscripts $n-1$ and n refer to the epoch number, whereas Δt stands for the time difference between the considered epochs.

Transition model for position and attitude related state parameters

For the position-velocity-acceleration (PVA) vectors, a constant acceleration is assumed in subsequent epochs. The resulting state transition model is then given by:

$$
\begin{bmatrix} \vec{b}_{13} \\ \vec{v}_1 \\ \vec{a}_1 \end{bmatrix}_n = \begin{bmatrix} \mathbf{I}_3 & \Delta t & \frac{\Delta t^2}{2} \\ \mathbf{0}_3 & \mathbf{I}_3 & \Delta t \\ \mathbf{0}_3 & \mathbf{0}_3 & \mathbf{I}_3 \end{bmatrix} \begin{bmatrix} \vec{b}_{13} \\ \vec{v}_1 \\ \vec{a}_1 \end{bmatrix}_{n-1} + \begin{bmatrix} \eta_x \\ \eta_v \\ \eta_a \end{bmatrix} \qquad (5.6)
$$

In case of the attitude state parameter transition, a constant angular rate is asumed. The resulting model can be described therefore by:

$$
\begin{bmatrix} \psi \\ \dot{\psi} \\ \theta \\ \dot{\theta} \\ \varphi \\ \dot{\varphi} \end{bmatrix}_n = \begin{bmatrix} \mathbf{I}_3 & \Delta t & \mathbf{0}_3 & \mathbf{0}_3 & \mathbf{0}_3 & \mathbf{0}_3 \\ \mathbf{0}_3 & \mathbf{I}_3 & \mathbf{0}_3 & \mathbf{0}_3 & \mathbf{0}_3 & \mathbf{0}_3 \\ \mathbf{0}_3 & \mathbf{0}_3 & \mathbf{I}_3 & \Delta t & \mathbf{0}_3 & \mathbf{0}_3 \\ \mathbf{0}_3 & \mathbf{0}_3 & \mathbf{0}_3 & \mathbf{I}_3 & \mathbf{0}_3 & \mathbf{0}_3 \\ \mathbf{0}_3 & \mathbf{0}_3 & \mathbf{0}_3 & \mathbf{0}_3 & \mathbf{I}_3 & \Delta t \\ \mathbf{0}_3 & \mathbf{0}_3 & \mathbf{0}_3 & \mathbf{0}_3 & \mathbf{0}_3 & \mathbf{I}_3 \end{bmatrix} \begin{bmatrix} \psi \\ \dot{\psi} \\ \theta \\ \dot{\theta} \\ \varphi \\ \dot{\varphi} \end{bmatrix}_{n-1} + \begin{bmatrix} \eta_\psi \\ \eta_{\dot{\psi}} \\ \eta_\theta \\ \eta_{\dot{\theta}} \\ \eta_\varphi \\ \eta_{\dot{\varphi}} \end{bmatrix} \qquad (5.7)
$$

The bias vectors both of the angular rate ($b_{\vec{\omega}}$) and acceleration measurement ($b_{\vec{a}}$) are instead assumed as constant.

Transition model for satellite-related state parameters

In case of the satellite-related parameters, these are varying relatively slowly over time, so that they are assumed all as constant over subsequent epochs. In particular, the sum of SD integer ambiguity and ionospheric delay $\lambda N_3^{\mathrm{sd}} + I^{\mathrm{sd}}$ is

Parameter	Description
$\lambda\phi_1^{\mathrm{sd}}$	Single-difference carrier phase measurement vector of receiver 1 [m]
$\lambda\phi_2^{\mathrm{sd}}$	Single-difference carrier phase measurement vector of receiver 2 [m]
ρ_1^{sd}	Single-difference code phase measurement vector of receiver 1 [m]
ρ_2^{sd}	Single-difference code phase measurement vector of receiver 2 [m]
f_{1d}^{sd}	Single-difference Doppler frequency measurement vector of receiver 1 [1/s]
f_{2d}^{sd}	Single-difference Doppler frequency measurement vector of receiver 2 [1/s]
$\vec{\omega}_{ib}^{b}$	Angular rate measurement vector in body-fixed frame [rad/s]
$\vec{a}^{b}$	3D-acceleration measurement vector in body-fixed frame [m/s^2]

Table 5.2: Description of the components of the measurement vector z

assumed to be quasi-constant, so that a very low value of process noise is chosen, whereas for the SD multipath error of both GNSS receiver 1 and 2 $\triangle\rho_{\mathrm{MP}1/2}^{\mathrm{sd}}$ a relatively higher process noise is chosen, in order to absorb short-time variations.

5.2.2 Measurement model

The measurement model describes how the single measurements of the sensor are related to the system's states. In general, for every epoch n, the measurement vector z_n, which contains all measured values, can be described as a function of the state vector x_n as:

$$z_n = h_n(x_n) + v_n \tag{5.8}$$

with h_n the (usually non-linear) function that relates one or more states with each measured value and v_n the measurement noise vector, which describes the expected noise variances of every measured value. As we are modeling an extended Kalman filter, h_n isn't linearized.

As for the process noise covariance matrix, the definition of the measurement noise covariance matrix follows as:

$$R_n = \mathbf{E}\left[v_n v_n^{\mathrm{T}}\right] \tag{5.9}$$

In our model, the measurement vector comprises the following measured values:

$$z_n = \left[\lambda\left(\tilde{\phi}_1^{\mathrm{sd}}\right)^{\mathrm{T}}, \lambda\left(\tilde{\phi}_2^{\mathrm{sd}}\right)^{\mathrm{T}}, \left(\tilde{\rho}_1^{\mathrm{sd}}\right)^{\mathrm{T}}, \left(\tilde{\rho}_1^{\mathrm{sd}}\right)^{\mathrm{T}}, \left(f_{1d}^{\mathrm{sd}}\right)^{\mathrm{T}}, \left(f_{2d}^{\mathrm{sd}}\right)^{\mathrm{T}}, \left(\vec{\omega}_{ib}^{b}\right)^{\mathrm{T}}, \left(\vec{a}^{b}\right)^{\mathrm{T}}\right]^{\mathrm{T}} \tag{5.10}$$

Table 5.2 explains the meaning of each component of the measurement vector.

As for the system model, only a subset of this measurement are available at a specific epoch, that because either GPS or IMU provided a measurement for that epoch. In order to select the available measurements from the whole measurement vector z_n, at each epoch n a similar selection operator as for the system model is applied, namely $s^z_n(\gamma_n,\, z_n)$. As before, γ_n denotes the sensor type (1 for GPS and 2 for IMU). The corresponding subsets of the measurement vector are described as follows:

$$
\begin{aligned}
s^z_n(1,\, z_n) &= \left[\lambda\left(\tilde{\phi}^{\mathrm{sd}}_1\right)^{\mathrm{T}},\, \lambda\left(\tilde{\phi}^{\mathrm{sd}}_2\right)^{\mathrm{T}},\, (\tilde{\rho}^{\mathrm{sd}}_1)^{\mathrm{T}},\, (\tilde{\rho}^{\mathrm{sd}}_1)^{\mathrm{T}},\, (f^{\mathrm{sd}}_{1d})^{\mathrm{T}},\, (f^{\mathrm{sd}}_{2d})^{\mathrm{T}}\right]^{\mathrm{T}} &(5.11)\\
s^z_n(2,\, z_n) &= \left[\left(\vec{\omega}^{\,b}_{ib}\right)^{\mathrm{T}},\, \left(\vec{a}^{b}\right)^{\mathrm{T}}\right]^{\mathrm{T}} &(5.12)
\end{aligned}
$$

Whereas the selection operator for the IMU-related measurements is in general selecting the same amount of measurements for every epoch, on GPS side, according to what has been said in the system model also, only the available single-difference measurements at each epoch n, coming from visible and tracked satellites, are selected.

Model for GNSS measurements

With reference to section 4.2, the individual single-difference corrected pseudorange measurements are modeled as:

$$
\begin{aligned}
\tilde{\rho}^{kl}_1 &= \rho^{kl}_1 - \left(\vec{e}^{\,kl}_1\right)^T \cdot \vec{r}_3 + \left(\vec{e}^{\,k}_1\right)^T \cdot \vec{r}^{\,k} - \left(\vec{e}^{\,l}_1\right)^T \cdot \vec{r}^{\,l} + c(\delta^k - \delta^l) - T^{kl}_1\\
&= (\vec{e}^{\,kl}_1)^T \cdot \vec{b}_{13} + \triangle\rho_{\mathrm{MP}}{}^{kl}_1 + I^{kl} + \eta^{kl}_1 &(5.13)
\end{aligned}
$$

$$
\begin{aligned}
\tilde{\rho}^{kl}_2 &= \rho^{kl}_2 - \left(\vec{e}^{\,kl}_1\right)^T \cdot \vec{r}_3 + \left(\vec{e}^{\,k}_1\right)^T \cdot \vec{r}^{\,k} - \left(\vec{e}^{\,l}_1\right)^T \cdot \vec{r}^{\,l} + c^{kl}_{12} + c(\delta^k - \delta^l) - T^{kl}_2\\
&= (\vec{e}^{\,kl}_1)^T(\vec{b}_{13} - \vec{b}_{12}) + \triangle\rho_{\mathrm{MP}}{}^{kl}_2 + I^{kl} + \eta^{kl}_2 &(5.14)
\end{aligned}
$$

$$
\begin{aligned}
\tilde{\rho}^{kl}_3 &= \rho^{kl}_3 - \left(\vec{e}^{\,kl}_1\right)^T \cdot \vec{r}_3 + \left(\vec{e}^{\,k}_1\right)^T \cdot \vec{r}^{\,k} - \left(\vec{e}^{\,l}_1\right)^T \cdot \vec{r}^{\,l} + c^{kl}_{13} + c(\delta^k - \delta^l) - T^{kl}_3\\
&= I^{kl} + \eta^{kl}_3 &(5.15)
\end{aligned}
$$

Putting every kl-satellite pair inside a vector, the above equation can be rewritten in matrix-vector notation as:

$$
\begin{aligned}
\tilde{\rho}^{\mathrm{sd}}_1 &= \mathbf{H}^{\mathrm{sd}}_1 \cdot \vec{b}_{13} + \triangle\rho_{\mathrm{MP}}{}^{\mathrm{sd}}_1 + \mathbf{I}^{\mathrm{sd}} + \eta_1{}^{\mathrm{sd}} &(5.16)\\
\tilde{\rho}^{\mathrm{sd}}_2 &= \mathbf{H}^{\mathrm{sd}}_1 \cdot (\vec{b}_{13} - \vec{b}_{12}) + \triangle\rho_{\mathrm{MP}}{}^{\mathrm{sd}}_2 + \mathbf{I}^{\mathrm{sd}} + \eta_2{}^{\mathrm{sd}} &(5.17)\\
\tilde{\rho}^{\mathrm{sd}}_3 &= \mathbf{I}^{\mathrm{sd}} + \eta_3{}^{\mathrm{sd}} &(5.18)
\end{aligned}
$$

Always having section 4.2 as reference, the individual single-difference corrected carrier phase measurements are modeled as:

$$
\begin{aligned}
\lambda\tilde{\phi}_1^{kl} &= \lambda\phi_1^{kl} - \left(\vec{e}_1^{\,kl}\right)^T \cdot \vec{r}_3 + \left(\vec{e}_1^{\,k}\right)^T \cdot \vec{r}^{\,k} - \left(\vec{e}_1^{\,l}\right)^T \cdot \vec{r}^{\,l} + c(\delta^k - \delta^l) - \lambda N_{13}^{kl} - T_1^{kl} \\
&= (\vec{e}_1^{\,kl})^T \cdot \vec{b}_{13} + \lambda N_3^{kl} - I^{kl} + \epsilon_1^{kl} \qquad (5.19)
\end{aligned}
$$

$$
\begin{aligned}
\lambda\tilde{\phi}_2^{kl} &= \lambda\phi_2^{kl} - \left(\vec{e}_1^{\,kl}\right)^T \cdot \vec{r}_3 + \left(\vec{e}_1^{\,k}\right)^T \cdot \vec{r}^{\,k} - \left(\vec{e}_1^{\,l}\right)^T \cdot \vec{r}^{\,l} + c_{12}^{kl} + c(\delta^k - \delta^l) - \ldots \\
&\quad \lambda N_{13}^{kl} + \lambda N_{12}^{kl} - T_2^{kl} \qquad (5.20) \\
&= (\vec{e}_1^{\,kl})^T (\vec{b}_{13} - \vec{b}_{12}) + \lambda N_3^{kl} - I^{kl} + \epsilon_2^{kl} \qquad (5.21)
\end{aligned}
$$

$$
\begin{aligned}
\lambda\tilde{\phi}_3^{kl} &= \lambda\phi_3^{kl} - \left(\vec{e}_1^{\,kl}\right)^T \cdot \vec{r}_3 + \left(\vec{e}_1^{\,k}\right)^T \cdot \vec{r}^{\,k} - \left(\vec{e}_1^{\,l}\right)^T \cdot \vec{r}^{\,l} + c_{13}^{kl} + c(\delta^k - \delta^l) - T_3^{kl} \\
&= \lambda N_3^{kl} - I^{kl} + \epsilon_3^{kl} \qquad (5.22)
\end{aligned}
$$

Again, the system of equation can be expressed in matrix-vector notation as:

$$
\begin{aligned}
\lambda\tilde{\phi}_1^{\text{sd}} &= \mathbf{H}_1^{\text{sd}} \cdot \vec{b}_{13} + \lambda \mathbf{N}_3^{\text{sd}} - \mathbf{I}^{\text{sd}} + \epsilon_1^{\text{sd}} \qquad (5.23) \\
\lambda\tilde{\phi}_2^{\text{sd}} &= \mathbf{H}_1^{\text{sd}} \cdot (\vec{b}_{13} - \vec{b}_{12}) + \lambda \mathbf{N}_3^{\text{sd}} - \mathbf{I}^{\text{sd}} + \epsilon_2^{\text{sd}} \qquad (5.24) \\
\lambda\tilde{\phi}_3^{\text{sd}} &= \lambda \mathbf{N}_3^{\text{sd}} - \mathbf{I}^{\text{sd}} + \epsilon_3^{\text{sd}} \qquad (5.25)
\end{aligned}
$$

Model for INS measurements

The measurement model for an INS-based KF update comprehends both the modeling of the body-fixed frame acceleration and angular rate measurements.

The body frame acceleration measurements are modeled as (the superscript refers to the coordinate frame):

$$
\begin{aligned}
\tilde{\vec{f}}^{\,b} &= \vec{a}^{\,b} + \vec{b}_a^{\,b} - \vec{g}^{\,b} + \eta_a \\
&= R_e^b\,(\vec{a}^{\,e} + 2\Omega_{ie}^e \vec{v}^{\,e}) + \vec{b}_a^{\,b} - R_n^b \vec{g}^{\,n} + \eta_a \qquad (5.26)
\end{aligned}
$$

where, as discussed in section 3.1.2, $\tilde{\vec{f}}^{\,b}$ represents the measured acceleration in body-fixed frame, $\vec{a}$ the true acceleration, $2\Omega_{ie}^e \vec{v}^e$ the Coriolis acceleration, $\vec{b}$ the bias error and $\vec{g}$ the gravity vector. η is modeled as Gaussian noise.

The body frame angular rate measurements are instead modeled as (superscript always refers to the coordinate frame):

$$
\begin{aligned}
\tilde{\vec{\omega}}_{ib}^b &= \vec{\omega}_{ib}^{\,b} + \vec{b}_\omega^{\,b} + \eta_\omega \\
&= \vec{\omega}_{ie}^{\,b} + \vec{\omega}_{en}^{\,b} + \vec{\omega}_{nb}^{\,b} + \vec{b}_\omega^{\,b} + \eta_\omega \qquad (5.27) \\
&= R_e^b(\vec{\omega}_{ie}^{\,e} + \vec{\omega}_{en}^{\,e}) + \left(\hat{R}_{\text{Euler}}\right)^{-1} \begin{bmatrix} \dot{\varphi} \\ \dot{\theta} \\ \dot{\psi} \end{bmatrix} + \vec{b}_\omega^b + \eta_\omega \qquad (5.28)
\end{aligned}
$$

where (see section 2.4) $\tilde{\vec{\omega}}_{ib}^{b}$ represents the measured angular rates, $\vec{\omega}_{ie}^{e}$ and $\vec{\omega}_{en}^{e}$ the angular rates describing the orientation changes between the inertial and ECEF frame and between the ECEF and NED frame, respectively. $\hat{R}_{\text{Euler}}$ stands for the estimated transformation matrix for Euler attitude rates, whereas $\dot{\varphi}$, $\dot{\theta}$ and $\dot{\psi}$ are the bank, elevation and heading Euler attitude rates, $\vec{b}_{\omega}$ the bias error and η is modeled, as usual, as Gaussian noise.

5.3 The Kalman Filter algorithm

The Kalman Filter algorithm is an iterative algorithm that comprises basically two alternating steps: the state prediction step and the state update step. In the first one, the system model is applied to predict the behavior of the system in the next epoch basing on a-priori information such as those coming from the movement model. In the second step, the update step, the prediction is confronted with the actual measurements, and a trade-off between the two estimates is chosen as optimal. This optimum is computed basing on the stochastic properties both of the state transition and measurement model with a Bayesian approach on a MMSE (minimum mean square error) basis.

One small clarification about the notations: in literature, all variables regarding the prediction step are denoted with minus sign as superscript, whereas the ones regarding the update step are denoted with a plus sign as superscript.

5.3.1 The prediction step

In the prediction step, the system model is used to make an estimate on the state variable's value for the subsequent epoch. In this phase, a prediction on the state parameter's values on the subsequent epoch is done only by assuming a linear model, such as a movement model. The equation that describes this prediction was already mentioned in Section 5.2.1, and it is repeated here for convenience:

$$\hat{x}_n^- = \Phi_{n-1}\hat{x}_{n-1}^+ \tag{5.29}$$

where $\hat{x}_{n-1}^+$ stands for the estimate of the state vector coming from the last update phase, namely those of epoch $n-1$, Φ_{n-1} the transition matrix of epoch $n-1$, $\hat{x}_n^-$ the estimate of the predicted state vector for the current epoch, namely n.

Together with the state vector, there is also another quantity that should be updated: namely the error covariance matrix, which is defined as the expected value of the state vector residuals, which in turn are defined as the difference or error between the real and estimated state vector:

$$P = \mathbf{E}\left[(x - \hat{x})(x - \hat{x})^{\mathrm{T}}\right] \tag{5.30}$$

where x is the true and $\hat{x}$ the estimated state vector. This matrix could be related either to the prediction or update step, in which case the matrix is called a-priori or a-posteriori error covariance matrix.

In the prediction step, the a-priori error covariance matrix P_n^- is updated as:

$$P_n^- = \Phi_{n-1} P_{n-1}^+ \Phi_{n-1}^{\mathrm{T}} + Q_{n-1} \tag{5.31}$$

where P_{n-1}^+, which represents the a-posteriori covariance matrix of the prior update step. One can observe here that the values of P_n^- could only have become bigger than the ones of P_{n-1}^+ (as long as the transition matrix Φ is not the identity matrix, which is usually never the case). This is consistent with the fact that in the prediction step no "real" information, such as a measured value, is given to the system, and thus the errors, and thus its (co)-variances, could only become bigger.

5.3.2 The update step

In this step, the measured values are taken into account and "fed back" to the system. As it has been mentioned in Section 5.2.1, the relationship between the state and measurement vector is:

$$z_n = h_n(x_n) + v_n \tag{5.32}$$

where $h_n(x_n)$ represents the measurement function and v_n the measurement noise vector. The non-linear measurement function $h_n(x_n)$ is linearized to the measurement matrix H_n as:

$$h_n(x_n) \approx H_n x_n \tag{5.33}$$

which is then used to calculate the Kalman gain matrix K_n and the a-posteriori covariance matrix P_n^+, as will be seen later in this section. The calculation of the measurement matrix can be then performed as:

$$H_n\big|_{x_n=x_0} = \frac{\partial}{\partial x_n} h_n(x_n)\bigg|_{x_n=x_0} \tag{5.34}$$

The update of the state vector is performed as:

$$\hat{x}_n^+ = \hat{x}_n^- + K_n(z_n - h_n(\hat{x}_n^-)) \tag{5.35}$$

where K_n stands for the Kalman gain matrix and the term $z_n - h_n(\hat{x}_n^-)$ is defined as measurement innovation, because it is the difference between the actual measured values z_n and the estimated state parameters from the prediction phase $\hat{x}_n^-$ transformed into the measurement space by $h_n(\hat{x}_n^-)$. This discrepancy between what the sensors are telling and what the linear model is pointing out is weighted by the Kalman gain matrix K_n and then finally added to the just calculated predicted state vector $\hat{x}_n^-$ coming from the last prediction phase.

The a-posteriori error covariance matrix is updated as follows:

$$P_n^+ = (I - K_n H_n) P_n^- \tag{5.36}$$

with I being the identity matrix, and K_n the Kalman gain matrix, which is defined as:

$$K_n = P_n^- H_n^{\mathrm{T}} (H_n P_n^- H_n^{\mathrm{T}} + R_n)^{-1} \tag{5.37}$$

The "updated" state vector $\hat{x}_n^+$ contains now state estimates that are optimal, considering both the new information provided by the measurements and the prediction of the linear model. This procedure should be iterated as long as new measurement data is available.[15, 1]

Chapter 6

Own contributions and measurement results

6.1 Improvements on static RTK positioning

Absolute positioning with centimeter level accuracy requires the use of the carrier phase measurements, which are characterized by centimeter level noise standard deviation. The carrier phase positioning requires the correct resolution of the integer ambiguities, as discussed in section 4.4. Moreover, we rely on double measurement differentiation to get rid of common both satellite related as well as receiver related error sources.

6.1.1 GNSS measurement set-up

To investigate the feasibility of integer ambiguity fixing on double difference level, we set up a measurement campaign using two low-cost GNSS antennas. Measurements have been taken by recording GPS pseudorange and carrier phase measurement simultaneously. We took measurements by putting the two antennas on various distances between each other, from a couple of meters up to about 100 meters. We performed the recordings in environments with very good to good satellite visibility and with relatively low possible multipath reflectors, in order to have a quite robust and error-free measurement pool. We successively performed artificial satellite removal and multipath injection to investigate the dependency of these occurrences with the quality of the fixing process.

Figure 6.1 shows a typical set-up of the GNSS antennas for one of the measurement sessions. According to Figure 5.1, the two GNSS antennas on the car's rooftop span the $\vec{b}_{12}$ baseline, which one can resolve for the Euler attitude angles to get the vehicle's orientation. The $\vec{b}_{13}$ baseline spanned between one rooftop antenna and the antenna on the tripod, instead, is able to position the car relatively to the static tripod antenna, and thus to absolutely position the car. The distance between the rooftop antennas was 1.02 meters, whereas the

Figure 6.1: Measurement session at Garching: detail of two GNSS u-blox antennas on the car rooftop (bottom-left) and of the third GNSS u-blox antenna on the tripod (bottom-right)

front-rooftop to tripod baseline measured 4.7 meters.

This measurement session took place at the student's parking lot of the TUM university campus at Garching, Munich. We wanted to have GNSS measurements with maximal sky visibility and mostly no multipath reflectors. Other measurement sessions have been made in similar conditions: one at Aschheim, Munich, near a cornfield, and another session has been performed at the Königsplatz, Munich. In these two other sessions we wanted to enlarge the spacing between the GNSS antennas so to raise the norm of the $\vec{b}_{13}$ baseline, so we putted the two antennas onto separate tripods. In Aschheim we performed a measurement session with a baseline length of more than 100 meters, whereas the one at the Königpslatz measured a little more than 15 meters. For all measurement sessions, the distances have been measured with a Leica DISTO™ laser distance-meter and used as a metric for evaluating the ambiguity fixing algorithm.

6.1.2 Fixing algorithm description

The developed algorithm performs integer ambiguity fixing on double difference level of a relative baseline between two low-cost GNSS receivers. We strongly rely on carrier phase measurement to achieve centimeter level accuracy.

Kalman Filter for float ambiguity estimation

The first step is to get a float estimation of the integer ambiguity. This can be done with a Kalman Filter that estimates the baseline, the float ambiguities and the code multipath by taking double difference code and phase measurements.

The state parameter vector can be defined as

$$x_n = \left[\left(\vec{b}_{12,\,n}\right)^{\mathrm{T}},\ \left(N^{sd}_{12,\,n}\right)^{\mathrm{T}},\ \left(\triangle\rho_{\mathrm{MP}}{}^{\mathrm{sd}}_{12,\,n}\right)^{\mathrm{T}}\right]^{\mathrm{T}}$$

The measurement vector consists of

$$z_n = \left[\left(\lambda\phi^{\mathrm{sd}}_{12,\,n}\right)^{\mathrm{T}},\ \left(\rho^{\mathrm{sd}}_{12,\,n}\right)^{\mathrm{T}}\right]^{\mathrm{T}}$$

The Kalman Filter is first initialized with a least-squares estimation of the baseline and float ambiguities as

$$\begin{bmatrix} \hat{\vec{b}}_{12} \\ \hat{N}^{sd}_{12} \end{bmatrix} = \left(G^{\mathrm{T}} R_1^{-1} G\right)^{-1} G^{\mathrm{T}} R_1^{-1} z_1 \tag{6.1}$$

where with

$$G = \begin{bmatrix} H^{\mathrm{sd}}_{\mathrm{ENU}} & \lambda\mathbf{I} \\ H^{\mathrm{sd}}_{\mathrm{ENU}} & \mathbf{0} \end{bmatrix}$$

it is meant the geometry matrix and R_1 stands for the measurement noise covariance matrix. The subscript refers to the epoch number, thus means that we are in the initialization epoch.

The float ambiguity residuals are then used to make a first estimation of the multipath parameter:

$$\begin{bmatrix} r_{\phi^{\mathrm{sd}}_{12}} \\ r_{\rho^{\mathrm{sd}}_{12}} \end{bmatrix} = z_1 - G\hat{x}_{\mathrm{LS}} \tag{6.2}$$

$$\triangle\hat{\rho}_{\mathrm{MP,init}}{}^{\mathrm{sd}}_{12} = r_{\rho^{\mathrm{sd}}_{12}} \tag{6.3}$$

where with $r_{\phi^{\mathrm{sd}}_{12}}$ and $r_{\rho^{\mathrm{sd}}_{12}}$ the double difference carrier phase and code phase measurement residuals of the least-squares estimation are respectively meant. The multipath parameter is initialized only with the code phase residuals. With this values the Kalman Filter is first initialized and then moved forward until the baseline estimation has reached a min-max stability given by:

$$\Delta b_{\mathrm{minmax}} = \max\left(\max\left(\vec{b}_{12}\left[n-N+1,\, n-N+2,\, \ldots,\, n\right]\right) - \ldots\right. \tag{6.4}$$

$$\left.\min\left(\vec{b}_{12}\left[n-N+1,\, n-N+2,\, \ldots,\, n\right]\right)\right) \tag{6.5}$$

where the maximum variation over a temporal window of the last N epochs is searched component by component. If this value falls below a threshold, the integer ambiguity fixing algorithm is started.

Integer collection phase

When the stability of the baseline estimation in the float KF defined in equation 6.4 reaches a first threshold, the integer collection phase is started. During this phase, the decorrelated set of integer ambiguities is estimated for every epoch using the LAMBDA algorithm introduced in section 4.4. This algorithm takes as input the float estimation of the ambiguities $\hat{N}$ performed with the float KF and its covariance matrix extracted from the Kalman filter's a-posteriori covariance matrix P_n^+ defined in section 5.3. This operation is repeated for every epoch, and all the unique candidate vectors are merged into a candidate pool matrix, which will be the set of integer candidate vectors that will be evaluated in the next phase.

Integer selection phase

During this phase, all the integer candidate vectors collected inside the pool are evaluated. For every epoch, the sum of squared error (SSE) of the phase measurement residuals are used as an evaluation criteria.

The double difference phase measurement residual for the i-th integer candidate is calculated as

$$r_{\phi,\,i} = \lambda \phi_{12}^{\mathrm{sd}} - H_{\mathrm{ENU}}^{\mathrm{sd}} \breve{\vec{b}}_{12,\,i} - \lambda \breve{N}_i \tag{6.6}$$

with

$$\breve{\vec{b}}_{12,\,i} = \left(\left(H_{\mathrm{ENU}}^{\mathrm{sd}} \right)^{\mathrm{T}} R_{\phi}^{-1} H_{\mathrm{ENU}}^{\mathrm{sd}} \right)^{-1} \left(H_{\mathrm{ENU}}^{\mathrm{sd}} \right)^{\mathrm{T}} \left(R_{\phi}^{-1} \lambda \left(\phi_{12}^{\mathrm{sd}} - \breve{N}_i \right) \right) \tag{6.7}$$

being the least-squares baseline estimate using the i-th integer candidate $\breve{N}_i$. R_ϕ stands for the double difference phase measurement covariance matrix. This baseline estimate is used to calculate the residuals of the phase measurement, which should be minimal if the actual integer candidate vector $\breve{N}_i$ is correct. In order to have a scalar parameter for measuring the magnitude of the residuals for each candidate vector, the SSE for each candidate is calculated as

$$\mathrm{SSE}_{\phi,\,i} = \left(\left(r_{\phi,\,i} \right)^{\mathrm{T}} R_{\phi}^{-1} r_{\phi,\,i} \right) / K \tag{6.8}$$

where K stands for the number of satellites and in the former equation the division serves as a normalization factor. This SSE value defined in equation 6.8 can be interpreted as the square of the ratio between the residual error defined in equation 6.6 and its uncertainty given by the square root of the phase covariance matrix R_ϕ. By setting a threshold for the SSE_ϕ of 10, we allow the ratio between error and uncertainty to grow up to $\sqrt{10} \approx 3,16$, that means that the actual residual error is allowed to be three times larger than its expected uncertainty.

For every selection epoch, the phase SSE of every candidate vector is calculated, and only the candidates having SSE below the threshold are selected as possibly correct candidates. If there are less than 10 candidates that fall below the SSE threshold, then the 10 "best" candidates, sorted by phase residual SSE, are selected, in order to have a minimum of 10 candidates to be further evaluated with our "best" candidate selection criteria presented in the next subsection.

"Best" candidate selection criteria

The candidates selected according to the previous subsection are then inspected over time. Therefore, we keep track of each least-squares baseline estimate for each candidate over time.

To simplify the expression and without much loss of generality, if one supposes a diagonal covariance matrix having unitary variance (thus $R_\phi = \mathbf{I}$) the least-squares baseline estimate in equation 6.7 can be rewritten as (in the following, the subscripts are dropped for simplicity):

$$\breve{b} = \left(H^{\mathrm{T}}H\right)^{-1} H^{\mathrm{T}} \left(\lambda\phi - \lambda\breve{N}\right) \tag{6.9}$$

As of equation 4.7, the double difference carrier phase measurement can be modeled as

$$\lambda\phi = Hb + \lambda N + \epsilon \tag{6.10}$$

where ϵ is modeled as Gaussian noise having, for simplicity, unitary variance. By defining

$$\epsilon' = \left(H^{\mathrm{T}}H\right)^{-1} H^{\mathrm{T}}\epsilon$$

and by substituting the expression of $\lambda\phi$ from equation 6.10 in equation 6.9 one can write

$$\begin{aligned} \breve{b} &= \left(H^{\mathrm{T}}H\right)^{-1} H^{\mathrm{T}} \left(Hb + \lambda\left(N - \breve{N}\right) + \epsilon\right) \\ &= b + \left(H^{\mathrm{T}}H\right)^{-1} H^{\mathrm{T}}\lambda\Delta N + \epsilon' \end{aligned}$$

where with ΔN we mean the error of the estimated integer candidate vector $\breve{N}$.

Now, if $\breve{b}$ is tracked over time for each candidate and supposing that the right candidate is inside the pool, it will happen that ΔN is zero for the right candidate. All other candidates will have $\Delta N \neq 0$, and thus its baseline estimates will vary over time due to the changing e-vectors inside the H-matrix. This will cause a slow drift of the baseline estimate that can be tracked by a least-squares linear fitting which can best model the quasi-linear drift of the e-vectors sinked into the Gaussian noise ϵ'.

The simple linear model (the subscript refers to the epoch number)

$$b_n = b_1 + (n-1)\,\Delta t \cdot \Delta b$$

can be written in vector-matrix form as

$$[b_1,\, b_2,\, \cdots,\, b_N]^{\mathrm{T}} = G \begin{bmatrix} b_1 \\ \Delta b \end{bmatrix}$$

having

$$G = \begin{bmatrix} 1 & 1 & \cdots & 1 \\ 0 & \Delta t & \cdots & (N-1)\,\Delta t \end{bmatrix}^{\mathrm{T}}$$

The slope of the baseline drift Δb can be best computed by a least-squares estimation.

The selected integer ambiguity candidates are then sorted by this baseline drift parameter. After waiting for a minimum number of epochs that are necessary to be able to observe the drift, the "best" candidate is chosen as the one having (1) a value of the phase SSE under a certain threshold; (2) the one showing lowest baseline drift and (3) the one having a drift at least a half so big as the second best candidate.

6.1.3 Fixing algorithm results

Baseline drift

Figure 6.2 shows the drift of the East component of the least-squares baseline estimate defined in equation 6.7 over time. The data is taken from the measurement session on the 100m baseline in Aschheim. One can clearly see that for the right candidate vector (candidate #1 in the figure) the drift is nearly absent (less than 5mm in 40 seconds), whereas candidate #11 and #90 show a noticeably increased drift over time. During the candidate selection process, all three candidates showed a reasonable measurement SSE, but in order to be able to distinguish the correct one, the least-square baseline temporal drift has to be taken into account.

The problem of distinguishing the right candidate becomes more clear if one takes a look at Figure 6.3, which shows a confront between the least-squares baseline drift and the SSE of the phase residuals over time for two selected candidates. The plots refer to the measurement session in Garching, performed with a baseline length of almost 5 meters. As one can see, the candidate #338 (the wrong one) shows a consecutively decreased phase residuals SSE. This can happen if the geometry accidentally allows a strong reduction of the measurement residual for "wrong" candidates, causing a low SSE value. But if one instead takes a look at the least-squares baseline drift, it shows the opposite picture: the baseline is almost not drifting for the correct candidate (#1), whereas for the "wrong" one (#338), it shows a drift of almost 4cm in 40 seconds.

The plots in Figure 6.3 prove that we are able to select the right candidate even when the measurement SSE doesn't allow a clear distinction.

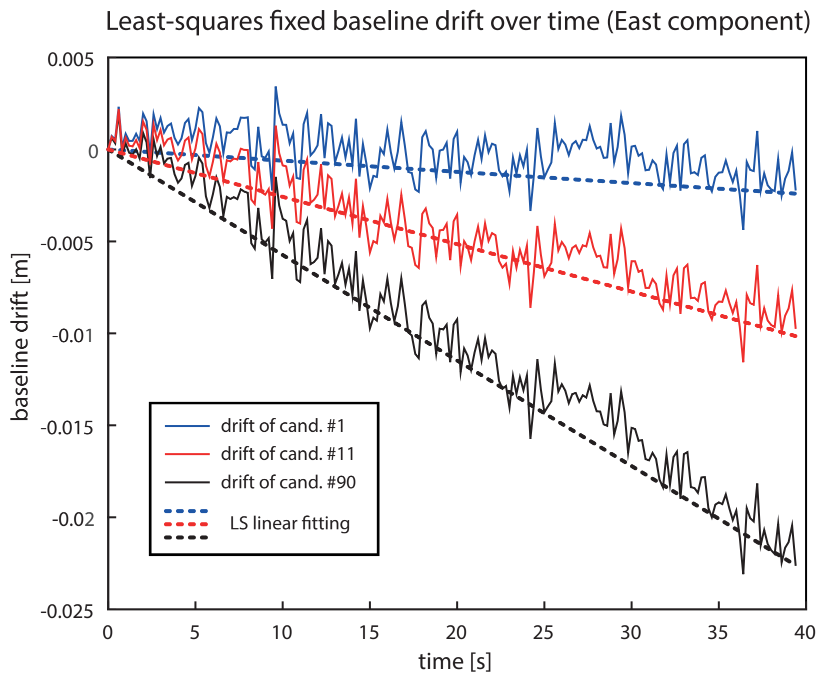

Figure 6.2: Least-squares baseline drift over time (East component) for the long-range 100 meter baseline recorded in Aschheim

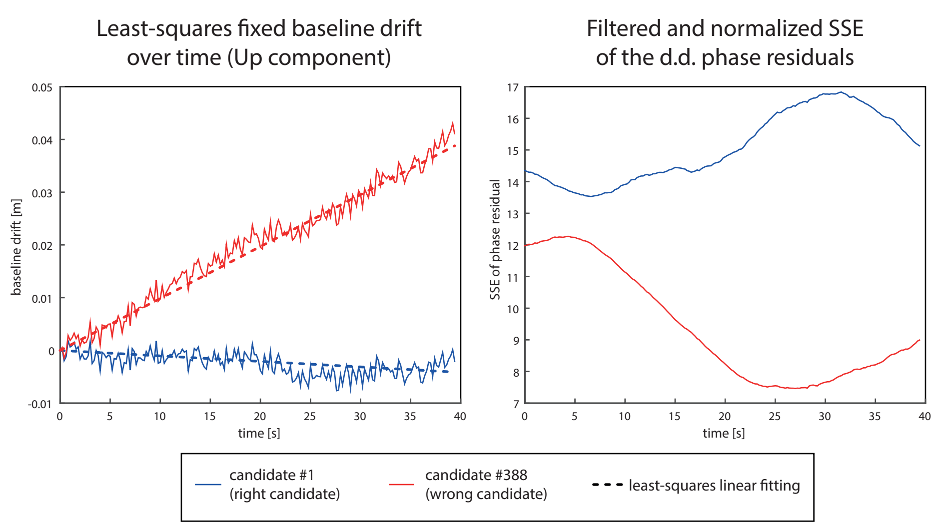

Figure 6.3: Confront of baseline drift (Up component) and filtered SSE of phase residuals for candidates #1 and #388, respectively; data coming from measurement session in Garching

time to fix [s]	length [m]	East [m]	North [m]	Up [m]	Head [deg]	Elev [deg]
124,6	104,1325	12,8940	103,3305	-0,3498	7,1129	-0,1925
103,0	104,1345	12,8950	103,3324	-0,3546	7,1132	-0,1951
103,6	104,1308	12,8960	103,3285	-0,3635	7,1141	-0,2000
113,0	104,1263	12,8993	103,3235	-0,3655	7,1162	-0,2011
100,6	104,1254	12,8994	103,3227	-0,3595	7,1163	-0,1978
111,6	104,1259	12,8991	103,3232	-0,3542	7,1161	-0,1949
99,6	104,1255	12,8974	103,3230	-0,3567	7,1152	-0,1963
199,4	98,0184	5,0177	97,4995	-8,7332	2,9461	-5,1117
118,6	104,1282	12,8919	103,3264	-0,3555	7,1120	-0,1956
112,4	104,1291	12,8897	103,3276	-0,3558	7,1107	-0,1958

Table 6.1: overview of the fixing results (columns 2 to 5 refer to the fixed baseline) for the long range baseline in Aschheim

Fixing results

The fixing algorithm has been run in post-processing mode using recorded GPS pseudorange and carrier phase measurements. The measurement sessions, as already said, have been performed with good to very good sky visibility and with possibly very low probability of signal reflectors to mitigate the multipath error. The GNSS antennas have been placed with various distances from each other, from about 5 to 100 meters. The algorithm iterates over the recorded measurement samples until it obtains a result, then it resets automatically and determines a new independent solution as long as there are more samples to process.

Table 6.1 shows the result in terms of estimated baseline after fixing the integer candidate vector, having on the respective columns from left to right the elapsed time for producing the result, the baseline length and its East, North and Up components in the local navigation frame as well as the computed heading and elevation attitude angles. The length of the baselines, corresponding to the distance between the two GNSS antennas, have been compared with the distance measurement performed with the laser distance meter, as said in section 6.1.1.

As one can see, the algorithm succeeded in outputting the right baseline estimation 9 out of 10 times, giving results with a uncertainty of about a centimeter.

To provide some statistical data, the fixing results are collected for all measurement sessions (Garching, Königsplatz and Aschheim). In the following, Table 6.2 shows an overview of the results in terms of number of independent results provided, the percentage of correct ambiguity fixing and the mean time it takes to provide a result. From the table we can see that the algorithm is able to find the correct integer candidate independently from the distance between the two antennas in about 90% of the time. Moreover, we can observe a correlation between the mean time to fix and the percentage of correct fixing: this is consistent with our baseline variation model where the baseline drift

measurement session	$\lVert\vec{b}\rVert$ [m]	results	success rate	mean t. to fix [s]
Aschheim, long range	104,13	10	90%	118,6
Aschheim, mid-range	16,81	8	87,5%	104,8
Garching, front-tripod	4,70	25	92%	141,4
Garching, rear-tripod	5,56	24	91,6%	142,2
Königsplatz, mid-range	13,89	8	100%	153,0

Table 6.2: Overview of number of results, success rate and time to fix for each measurement session

parameter	results	standard dev.
baseline East comp.	63	0,0027 m
baseline North comp.	63	0,0059 m
baseline Up comp.	63	0,0044m
baseline length	63	0,0113 m
attitude Heading angle	61	0,0300 deg
attitude Elev. angle	61	0,0390 deg

Table 6.3: statistics of the baseline estimate variation over all measurement sessions (outliers have been removed)

observability increases with the time of observation.

In order to evaluate the repeatability of the successive fixing results, the standard deviation from the correct result has been calculated, putting together all results provided in each measurement session. To calculate this standard deviation, first the outliers (or incorrect fixes) have been excluded, then the mean of each result parameter has been subtracted separately for each measurement session.

Table 6.3 shows the standard deviation of each baseline component, the baseline length and the attitude angles, once that the mean has been subtracted. As one can see, the standard deviation of the three baseline components remains in the order of millimeters, the one of the length parameter remains in the order of one centimeter, whereas for the attitude angles the mean deviation is less than 0,05 degrees.

Figure 6.4 and Figure 6.5 present histogram plots of the baseline's component in the local East-North-Up navigation frame and of the attitude angles, respectively. As for table 6.3, the incorrect results have been excluded from the plots.

Results show that we are able to fix to the correct ambiguity candidate mostly independently from the baseline length in about 9 out of 10 times achieving centimeter-level accuracy thanks to carrier phase positioning. The measurements has been taken in environments with good to very good sky visibility and with possibly very low probability of multipath reflectors. The fixing algorithm has been also tested with artificially injected code phase multipath error modeled as a random-walk process and with artificial measurement outages, where

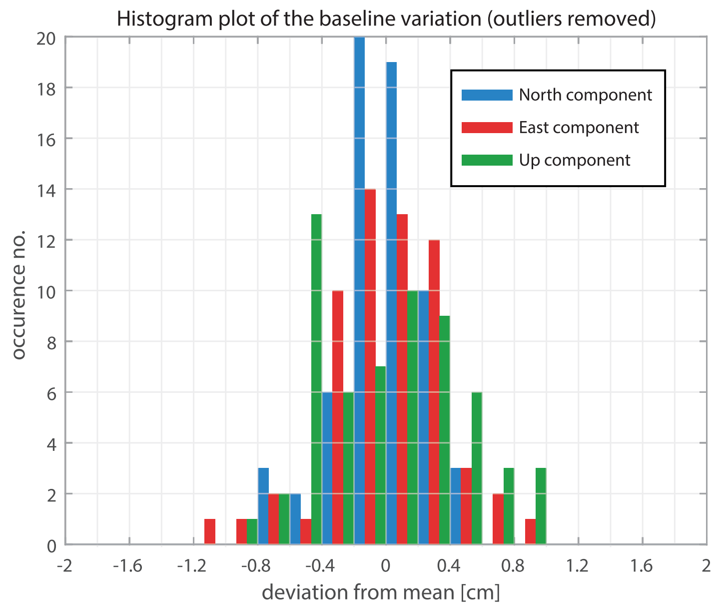

Figure 6.4: Histogram plot of the baseline deviation for each component from the mean value (outliers have been removed)

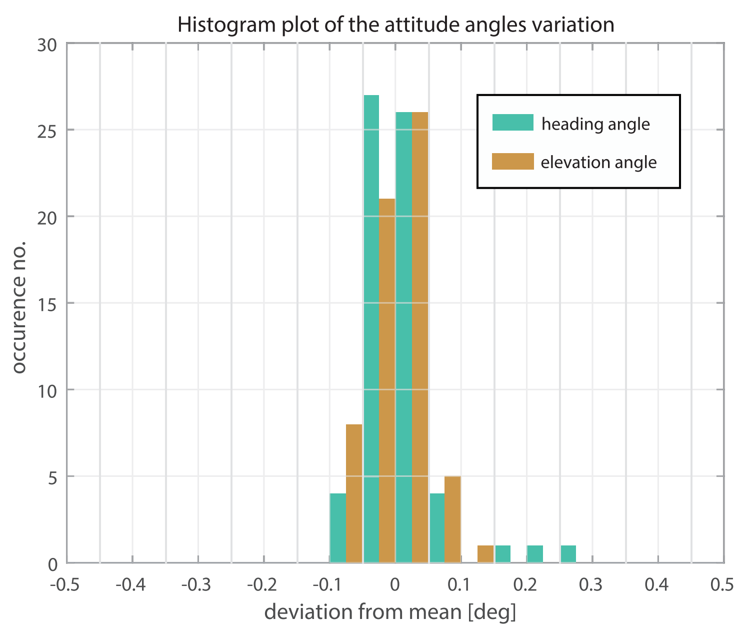

Figure 6.5: Histogram plot of the attitude angle's deviation from the mean value (outliers have been removed)

we reduced the number of available measurements for the whole fixing process. The correct fixing success ratio seems to be rather independent from code phase multipath injection but showed some dependency on the number of available carrier phase measurements: in case of reduced measurement availability, the drift of the baseline components becomes less evident, lowering the evidence of the correct integer ambiguity candidate.

Regarding the success rate introduced in table 6.2, the incorrect fixes may have two major causes: (1) the variability of the carrier phase measurement covariance matrix R_ϕ may scale the least-squares estimation of the baseline (see equation 6.7) differently for each epoch, and (2) the unmodeled carrier phase multipath error could reshape the temporal variation of the least-squares baseline estimation such that linear regression becomes not feasible. Possible improvements against this drawbacks may lie in case of (1) to consider a constant phase measurement covariance matrix during the baseline tracking epochs in order to avoid heterogeneous error scaling, and in case of (2) to model, along with code phase multipath error, a separate carrier phase multipath error parameter in the float Kalman Filter.

6.2 Refinements on the inertial sensor model

In this section, the enhancements on the mathematical model that characterizes the inertial measurements shall be outlined. We designed an INS mechanization in the Earth-centered Earth-fixed (ECEF) frame, the latter being the coordinate frame in which we estimate the position, velocity and acceleration parameters in our Kalman Filter approach. Therefore, particular attention has to be made when estimating the rotation matrix from the sensor related body-fixed frame to the mechanization related ECEF frame.

6.2.1 Calibration and first-order bias estimation

The inertial sensor is first calibrated with help of the GNSS-based attitude computation thanks to the two GNSS antennas on the car rooftop. With reference on Figure 5.1, the baseline $\vec{b}_{12}$ can be expressed in the body-fixed frame having only the first component unequal to zero, as it is spanned on the vehicle's longitudinal axis. Rotating the baseline into the NED navigation frame yields:

$$\vec{b}^b_{12} = [b_l,\, 0,\, 0]^{\mathrm{T}} \tag{6.11}$$

$$\begin{aligned}
\vec{b}^n_{12} &= R^n_b \vec{b}^b_{12} \\
&= R_3(-\psi)R_2(-\theta)R_1(-\varphi)\vec{b}^b_{12} \\
\begin{bmatrix} b_N \\ b_E \\ b_D \end{bmatrix} &= \begin{bmatrix} b_l\cos(\psi)\cos(\theta) \\ b_l\sin(\psi)\cos(\theta) \\ -b_l\sin(\theta) \end{bmatrix}
\end{aligned} \tag{6.12}$$

where b_l stands for the fix baseline length. Solving equation set 6.12 for the attitude angles $\psi$and θ yields

$$\hat{\psi} = \arctan\left(\frac{\hat{b}_E}{\hat{b}_N}\right) \tag{6.13}$$

$$\hat{\theta} = \arctan\left(\frac{-\hat{b}_D}{\sqrt{\left(\hat{b}_N\right)^2 + \left(\hat{b}_E\right)^2}}\right) \tag{6.14}$$

Once that the baseline estimation is performed using ambiguity-fixed GNSS carrier phase measurements, the attitude angles can be extracted and used for initializing the inertial sensor. The two-antenna set-up of the GNSS sensor part permits a very precise initialization of the attitude angles, and the ambiguity fixing can be done with high reliability if the length of the baseline is known[16]. It has to be noted though that due to the along-track alignment of the baseline, the latter is invariant to rotation along this axis, and thus its expression in the NED frame independent from the roll attitude angle φ. Although in car navigation the sensor are mostly aligned on a flat terrain and thus both θ and φ can be assumed as zero, for some applications this may not be true. The only way to get a rough estimate of the roll angle is by using the gravity vector.

Similarly as for the baseline vector in the body frame, the gravity vector in the navigation frame has only the Down component which is unequal to zero, and rotating it back to the body frame yields

$$\vec{g}^{\,n} = [0,\, 0,\, g]^{\mathrm{T}} \tag{6.15}$$

$$\vec{g}^{\,b} = R_n^b \vec{g}^{\,b} \tag{6.16}$$

$$= R_1(\varphi)R_2(\theta)R_3(\psi)\vec{g}^{\,b} \tag{6.17}$$

$$\begin{bmatrix} g_X \\ g_Y \\ g_Z \end{bmatrix} = \begin{bmatrix} -g\sin(\theta) \\ \sin(\varphi)\cos(\theta) \\ \cos(\varphi)\cos(\theta) \end{bmatrix} \tag{6.18}$$

The rough estimation of the roll angle can be performed as

$$\hat{\varphi} = \arctan\left(\frac{f_Y}{f_X}\right) \tag{6.19}$$

Where with f_X and f_Y it is meant the first and second components of the measured acceleration of the accelerometers during the calibration phase, when the vehicle is not moving. This model is not accurate due to the accelerometer biases, but is a simple and robust solution to get the third attitude angle that otherwise would have been just assumed equal to zero.

The first-order bias estimation is then simply done by integrating both the angular rate and acceleration values once. One can observe a linear trend that corresponds to the bias offset in the former values. For every epoch n, the values are integrated as

$$\begin{aligned} \Delta\vec{a}_{n+1} &= \vec{f}_n - \vec{g}_n + (t_n - t_{n-1})\,\Delta\vec{a}_n && (6.20) \\ \Delta\vec{\omega}_{n+1} &= \vec{\omega}_n + (t_n - t_{n-1})\,\Delta\vec{\omega}_n && (6.21) \end{aligned}$$

where with $\Delta\vec{a}$ and $\Delta\vec{\omega}$ the integrated acceleration and angular rates are respectively meant. Once that all calibration epochs are processed, linear regression is performed to optimally get the linear trend from the noisy measurements. The linear regression is simply performed as

$$\begin{aligned} \begin{bmatrix} \hat{\vec{a}}_1 \\ \Delta\hat{\vec{a}} \end{bmatrix} &= \left(G^{\mathrm{T}}G\right)^{-1} G^{\mathrm{T}}\Delta\vec{a} && (6.22) \\ \begin{bmatrix} \hat{\vec{\omega}}_1 \\ \Delta\hat{\vec{\omega}} \end{bmatrix} &= \left(G^{\mathrm{T}}G\right)^{-1} G^{\mathrm{T}}\Delta\vec{\omega} && (6.23) \end{aligned}$$

having

$$G = \begin{bmatrix} 1 & 1 & \cdots & 1 \\ 0 & t_2 - t_1 & \cdots & t_N - t_1 \end{bmatrix}^{\mathrm{T}}$$

The estimated least-squares linear slopes $\Delta\hat{\vec{a}}$ and $\Delta\hat{\vec{\omega}}$ can be directly used to initialize the acceleration and angular rate biases, respectively.

Figure 6.6 shows, for each accelerometer measurement, the integrated accelerations during the calibration phase (when the car is standing) once that the gravity vector has been subtracted. The dashed lines represent the linear least-squares regression that has been performed to extract the first order bias. As one can see, the curves fit very well for with the linear model, and this confirms the pertinence of the model for first-order bias estimation, as this is mainly the dominant error in low-cost INS sensors. But this is unfortunately not enough for estimating precisely the acceleration biases. Another factor that could reduce the accuracy in the bias estimation is the correct calculation of the gravity vector, which implies also the correct calculation of the attitude angles, in order to correctly rotate the vector into the body-fixed frame. However, this bias estimation method should be sufficiently accurate for our purposes.

6.2.2 Improvements on the mathematical model

As already mentioned earlier in this work, one of the key points in inertial navigation is the correct rotation from the body-fixed frame into the coordinate frame in which the tight coupling is mechanized (in our case it is the ECEF-frame). This involves the correct estimation, for every epoch, of the respective

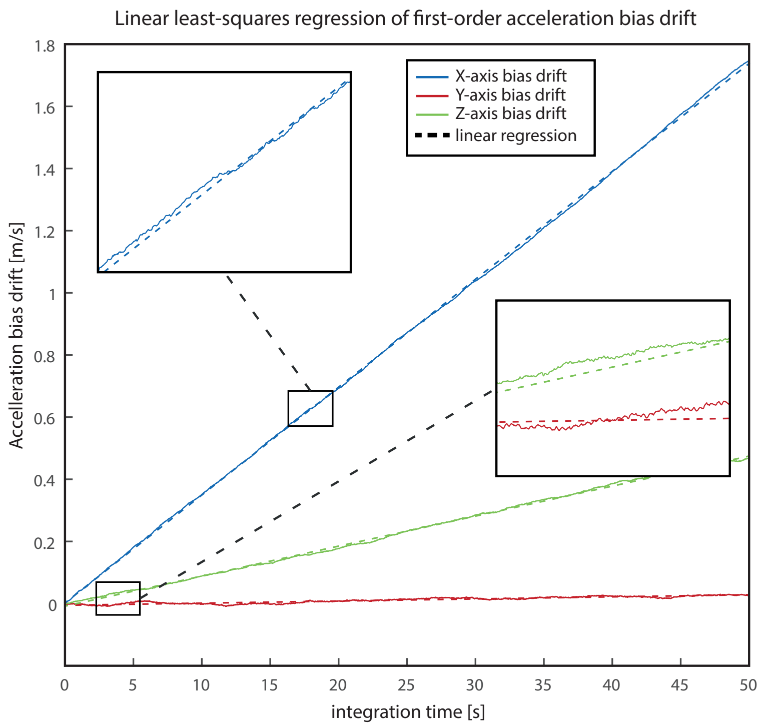

Figure 6.6: Acceleration bias drift during calibration phase

rotation matrix. Besides improving the mathematical formula to estimate this rotation matrix, other small effects like the Coriolis acceleration has been considered and corrected inside the code.

Acceleration measurement model

As already mentioned in section 5.2.2, the acceleration measurements are modeled as

$$\tilde{\vec{f}}^{\,b} \quad = \quad R_e^b \left(\vec{a}^{\,e} + 2\Omega_{ie}^{\,e} \vec{v}^{\,e} \right) + \vec{b}_a^{\,b} - R_n^b \vec{g}^{\,n} + \eta_a \tag{6.24}$$

where $\tilde{\vec{f}}^{\,b}$ is the measured acceleration in the body-fixed frame, $\vec{a}^{\,e}$ and $\vec{v}^{\,e}$ are the acceleration and velocity, respectively, of the vehicle in the ECEF frame, $2\Omega_{ie}^{\,e}\vec{v}^{\,e}$ is the Coriolis acceleration expressed in the ECEF frame, $\vec{b}_a^{\,b}$ are the accelerometer biases in the body frame, $\vec{g}^{\,n}$ is the gravity vector given in the NED frame, and η_a is modeled as Gaussian noise.

Taking to the left side the known terms, equation 6.24 becomes:

$$\begin{aligned} \tilde{\vec{f}}^{b}_{\text{corr}} &= \tilde{\vec{f}}^{\,b} - 2R_e^b \Omega_{ie}^{\,e} \vec{v}^{\,e} - R_n^b \vec{g}^{\,n} \\ &= R_e^b \vec{a}^{\,e} + \vec{b}_a^{\,b} + \eta_a \end{aligned}$$

in which the rotated Coriolis acceleration and gravity vector has been subtracted from the raw measurements.

Angular rate measurement model

Again, as written in section 5.2.2, the angular rate measurements are modeled as

$$\tilde{\vec{\omega}}_{ib}^{\,b} \quad = \quad R_e^b (\vec{\omega}_{ie}^{\,e} + \vec{\omega}_{en}^{\,e}) + \left(\hat{R}_{\text{Euler}} \right)^{-1} \begin{bmatrix} \dot{\varphi} \\ \dot{\theta} \\ \dot{\psi} \end{bmatrix} + \vec{b}_\omega^{\,b} + \eta_\omega \tag{6.25}$$

where $\tilde{\vec{\omega}}_{ib}^{\,b}$ are the angular rates measured by the gyroscopes, $\vec{\omega}_{ie}^{\,e}$ and $\vec{\omega}_{en}^{\,e}$ are the angular rates of the ECEF frame w.r.t. inertial frame and of the navigation frame w.r.t. the ECEF frame, respectively, $\hat{R}_{\text{Euler}}$ is the estimated Euler matrix (see section 2.4), $\dot{\varphi}$, $\dot{\theta}$ and $\dot{\psi}$ are the time derivatives of the Euler attitude angles which we estimate in our Kalman Filter, $\vec{b}_\omega^{\,b}$ are the angular rate bias errors and η_ω is modeled as Gaussian noise.

Taking to the left side the known term yields

$$\begin{aligned} \tilde{\vec{\omega}}^{b}_{ib,\,\text{corr}} &= \tilde{\vec{\omega}}^{b}_{ib} - R_e^b (\vec{\omega}_{ie}^{\,e} + \vec{\omega}_{en}^{\,e}) \\ &= \left(\hat{R}_{\text{Euler}} \right)^{-1} \begin{bmatrix} \dot{\varphi} \\ \dot{\theta} \\ \dot{\psi} \end{bmatrix} + \vec{b}^{b}_\omega + \eta_\omega \end{aligned}$$

where the known angular rates are subtracted from the gyro measurements.

Estimation of the ECEF-to-body frame rotation matrix in closed form

With reference to section 2.3, equation 2.5, in case of ECEF-to-body coordinate frame rotation, can be written as

$$\dot{R}_b^e = R_b^e \Omega_{eb}^b \tag{6.26}$$

where Ω_{eb}^b is the skew-symmetric matrix of $\vec{\omega}_{eb}^b$. This first-order differential equation can be solved in closed form.

Any first-order differential equation of the form

$$\frac{dy}{dt} = yt$$

can be solved explicitly for the time interval $\Delta t = [t_1\, t_2]$ as

$$\frac{y(t_2)}{y(t_1)} = e^{\int_{t_1}^{t_2} x \cdot dt}$$

if Δt is small enough, one can assume x as constant during this interval. By defining $y(t_n) = y_n$ one can write the differential equation in recursive form as

$$\begin{aligned} y_{n+1} &= y_n e^{x\Delta t} \\ &= y_n \sum_{p=0}^{\infty} \frac{(x\Delta t)^p}{p!} \end{aligned}$$

where the expression of the exponential function as infinite power series has been used. Plugging back the above expression into equation 6.26 yields (in the following, for simplicity, the indexes of the coordinate frames will be dropped)

$$R_{n+1} = R_n \sum_{p=0}^{\infty} \frac{S^p}{p!} \tag{6.27}$$

where

$$S = \Omega \Delta t$$

is the skew-symmetric matrix describing the small angle displacement in the relatively small time interval Δt. As a 3-by-3 skew-symmetric matrix,S has the following properties:

$$\begin{cases} S^k = (-1)^{\left\lfloor \frac{k-1}{2} \right\rfloor} |\theta|^{k-1} S; & k \geq 3;\, k\,\text{odd} \\ S^k = (-1)^{\left\lfloor \frac{k-1}{2} \right\rfloor} |\theta|^{k-2} S^2 & k \geq 4;\, k\,\text{even} \end{cases}$$

where with $\lfloor \bullet \rfloor$ it is meant the lower integer part of $\bullet$ and

$$|\theta| = \|\vec{\omega}\Delta t\|$$

Equation 6.27 can be expanded and rearranged as

$$\begin{aligned} R_{n+1} &= R_n \left[\mathbf{I}_3 + \left(\frac{1}{2!} - \frac{1}{4!}|\theta|^2 + \frac{1}{6!}|\theta|^4 - \cdots \right) S^2 + \ldots \right. \\ & \left. \left(1 - \frac{1}{3!}|\theta|^3 + \frac{1}{5!}|\theta|^5 - \cdots \right) S \right] \\ &= R_n \left[\mathbf{I}_3 + \left(\sum_{n=1}^{\infty} \frac{(-1)^{n-1}|\theta|^{2(n-1)}}{(2n)!} \right) S^2 + \ldots \right. \\ & \left. \left(\sum_{n=0}^{\infty} \frac{(-1)^n |\theta|^{2n}}{(2n)!} \right) S \right] \end{aligned} \tag{6.28}$$

Now, by expressing the sine and cosine functions as infinite power series, one can write:

$$\begin{aligned} \frac{\sin(x)}{x} &= \sum_{n=0}^{\infty} \frac{(-1)^n x^{2n}}{(2n)!} \\ \frac{1-\cos(x)}{x^2} &= \sum_{n=1}^{\infty} \frac{(-1)^{n-1} x^{2(n-1)}}{(2n)!} \end{aligned}$$

and thus rewrite equation 6.28 as:

$$R_{n+1} = R_n \left(1 + \frac{\sin(|\theta|)}{|\theta|} S + \frac{1-\cos(|\theta|)}{|\theta|^2} S^2 \right) \tag{6.29}$$

in which the updated rotation matrix R_{n+1} can be computed from its previous update R_n and the linearized small angle variations described in S and $|\theta|$ [2]. This gives a recursive and closed form solution for differential equation 6.26, and corresponds in literature to the matrix notation of the Rodriguez formula[17].

Now, back to equation 6.26, the angular rate vector $\vec{\omega}_{be}^e$ can be split as

$$\begin{aligned} \vec{\omega}_{eb}^b &= \vec{\omega}_{ib}^b - \vec{\omega}_{ie}^b \\ &= \vec{\omega}_{ib}^b - R_e^b \vec{\omega}_{ie}^e \end{aligned} \tag{6.30}$$

where $\vec{\omega}_{ib}^b$ is the angular rate sensed by the gyroscopes and $\vec{\omega}_{ie}^e$ is the angular rate referred to Earth rotation and can be easily expressed as

$$\vec{\omega}_{ie}^e = [0,\, 0,\, \omega_e]^{\mathrm{T}}$$

having with ω_e the Earth rotation rate in rad/s.

The rotation matrix R_e^b from equation 6.30 can be updated using equation 6.29 by letting

$$S = \Omega_{eb}^b \Delta t$$

and

$$|\theta| = \left\| \vec{\omega}_{eb}^b \Delta t \right\|$$

R_e^b can then be used in both the acceleration measurement model (equation 6.24) and the angular rate measurement model (equation 6.25). This closed form estimation of the rotation matrix gives a very precise result, thus increasing the accuracy of the model itself. The only two assumed approximations are (1) that the angular rate $\vec{\omega}_{eb}^b$ is constant over the interval Δt and (2) that $\left[R_e^b \vec{\omega}_{ie}^e\right]_n \approx \left[R_e^b \vec{\omega}_{ie}^e\right]_{n+1}$ (n refers to the epoch index), which is admissible because of the relatively small magnitude of $\vec{\omega}_{ie}^e$ itself.

Estimation of the Euler matrix

As already mentioned in section 2.4, the so-defined called Euler matrix describes the differential nonlinear relationship between the angular rate of the body frame w.r.t. the navigation frame ($\vec{\omega}_{nb}^b$) and the time derivative of the Euler attitude angles. The Euler matrix can be approximated using the previous estimation of the attitude angles. Denote with n the epoch number, the approximated Euler matrix can be computed as

$$\hat{R}_n^{\text{Euler}} = \begin{bmatrix} 1 & \sin(\hat{\varphi}_{n-1})\tan(\hat{\theta}_{n-1}) & \cos(\hat{\varphi}_{n-1})\tan(\hat{\theta}_{n-1}) \\ 0 & \cos(\hat{\varphi}_{n-1}) & -\sin(\hat{\varphi}_{n-1}) \\ 0 & \sin(\hat{\varphi}_{n-1})\sec(\hat{\theta}_{n-1}) & \cos(\hat{\varphi}_{n-1})\sec(\hat{\theta}_{n-1}) \end{bmatrix} \tag{6.31}$$

where $\hat{\varphi}$and $\hat{\theta}$ are the roll and elevation angle estimates coming from the last update of the KF state vector. With this approximation we get

$$\vec{\omega}_{nb}^b \approx \left(\hat{R}_n^{\text{Euler}}\right)^{-1} \begin{bmatrix} \dot{\varphi} \\ \dot{\theta} \\ \dot{\psi} \end{bmatrix} \tag{6.32}$$

which is a linearized relationship between $\vec{\omega}_{nb}^b$ and the Euler attitude rates that can be used in the angular rate measurement model of equation 6.25.

Estimation of the navigation frame w.r.t. ECEF frame angular rate vector

As one can see from equation 6.25, the mathematical model for the angular rates involves the estimation of the angular rate vector $\vec{\omega}_{en}^e$, which has to be given in coordinates in the ECEF frame.

Let's start with defining the navigation w.r.t. ECEF frame angular rotation vector with coordinates given in the NED navigation frame, for which we reference to [2]:

$$\vec{\omega}_{en}^{n} = \begin{bmatrix} \frac{v_E}{R_N+h} \\ -\frac{v_N}{R_M+h} \\ -\frac{v_E \tan\phi}{R_N+h} \end{bmatrix} \tag{6.33}$$

having, with

$$R_N = \frac{a}{\left(1-e^2\sin^2\phi\right)^{\frac{1}{2}}}$$

the normal Earth radius; with

$$R_M = \frac{a\left(1-e^2\right)}{\left(1-e^2\sin^2\phi\right)^{\frac{3}{2}}}$$

the meridian Earth radius and h stands for the height from the Earth ellipsoid surface (all quantities are in meters); a and e stand for the Earth ellipsoid semi-major axis and eccentricity, respectively, whereas with ϕ it is meant the latitude in radians.

Now we have to find an expression for v_E and v_N, which are the East and North velocities in the NED frame, that are function of the velocities in the ECEF frame, which is our reference frame for KF mechanization.

This is easily done by involving the ECEF-to-NED rotation matrix defined in section 2.2.2:

$$\begin{aligned} \vec{v}^{\,n} &= R_e^n \vec{v}^{\,e} \\ \begin{bmatrix} v_N \\ v_E \\ v_D \end{bmatrix} &= R_2(-\phi-\frac{\pi}{2})R_3(\lambda)\begin{bmatrix} v_X \\ v_Y \\ v_Z \end{bmatrix} \end{aligned}$$

which yields

$$\begin{aligned} v_N &= v_Z\cos\phi - \sin\phi\left(v_Y\sin\lambda + v_X\cos\lambda\right) \\ v_E &= v_Y\cos\lambda - v_X\sin\lambda \end{aligned}$$

Plugging in the obtained expressions of v_N and v_E into equation 6.33 and rotating back to ECEF frame yields

$$
\begin{aligned}
\vec{\omega}^e_{en} &= R^e_n \vec{\omega}^n_{en} && (6.34)\\
&= R_3(-\lambda) R_2(\frac{\pi}{2}+\phi) \begin{bmatrix} \frac{v_E}{R_N+h} \\ -\frac{v_N}{R_M+h} \\ -\frac{v_E \tan\phi}{R_N+h} \end{bmatrix} \\
&= \begin{bmatrix} -\sin\phi\cos\lambda & -\sin\lambda & -\cos\phi\cos\lambda \\ -\sin\phi\sin\lambda & \cos\lambda & -\cos\phi\sin\lambda \\ \cos\phi & 0 & -\sin\lambda \end{bmatrix} \begin{bmatrix} \frac{v_Y\cos\lambda - v_X\sin\lambda}{R_N+h} \\ -\frac{v_Z\cos\phi - \sin\phi(v_Y\sin\lambda + v_X\cos\lambda)}{R_M+h} \\ -\frac{(v_Y\cos\lambda - v_X\sin\lambda)\tan\phi}{R_N+h} \end{bmatrix} \\
&= \begin{bmatrix} \frac{\sin\lambda[\sin\phi(v_X\cos\lambda + v_Y\sin\lambda) - v_Z\cos\phi]}{R_M+h} \\ \frac{\cos\lambda[\sin\phi(v_X\cos\lambda + v_Y\sin\lambda) - v_Z\cos\phi]}{R_M+h} \\ -\frac{v_X\sin\lambda - v_Y\cos\lambda}{\cos\phi(R_N+h)} \end{bmatrix}
\end{aligned}
$$

that gives us an explicit expression of $\vec{\omega}^e_{en}$ as a function of the ECEF velocities v_X, v_Y and v_Z; the geodetic longitude λ and latitude ϕ and of R_M, R_N and h. This expression can be plugged into equation 6.25 to correct for the body-to-navigation frame angular rate.

6.2.3 Corrections due to displacement and misalignment of GNSS-centered and INS-centered body frame

In our sensor set-up, the physical displacement of the INS sensor plate an the two GNSS antenna on the car rooftop implies a different origin of the body-fixed coordinate frames: one is defined as the phase center of the first GNSS antenna and is aligned with the resulting baseline $\vec{b}_{12}$, whereas the other is defined as the center of the axes spanned by the three gyroscopes and accelerometers of the INS sensor plate. As one can see from Figure 6.7, which shows the physical placement of the sensors in the test vehicle that has been used for tight coupling, the INS sensors are placed near the handbrake structure, whereas the two GNSS antennas are placed on the car rooftop, aligned with the along-track vehicle's middle axis.

Corrections for the sensor displacement: the lever-arm effect

The displacement of the INS sensor plate w.r.t. the phase center of the first GNSS antenna causes that the acceleration values sensed by the accelerometers doesn't match with the one's sensed on the GNSS antenna. Because the latter is our reference origin point of the body-fixed frame, one has to calculate the corresponding acceleration values on the origin as a function of the IMU-measured accelerations and angular rates.

Assuming the vehicle as a rigid body, so that the two body-fixed coordinate frames remain at a fixed distance and orientation from each other, and defining as $\mathbf{0}_{\text{GPS}}$ and $\mathbf{0}_{\text{IMU}}$ as their respective origin points and taking $\mathbf{0}_{\text{Inertial}}$ as the origin of an inertial frame (see Figure 6.8), the position of the INS sensor plate $\mathbf{0}_{\text{IMU}}$ can be written as:

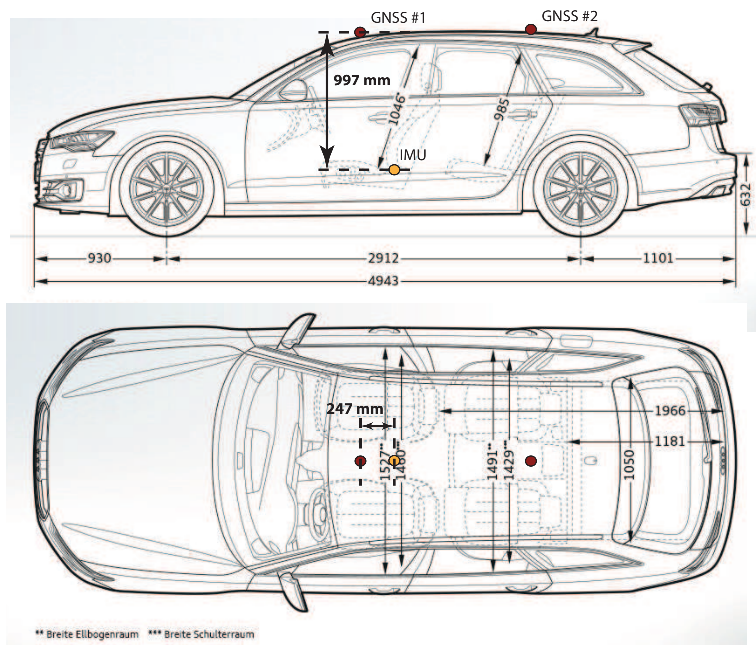

Figure 6.7: Audi A6 Avant GNSS antennas and INS sensor placement

$$
\begin{aligned}
\vec{x}^i_{\mathrm{GPS}} &= \vec{x}^i_{\mathrm{IMU}} + \vec{b}^i_{\mathrm{IG}} && (6.35)\\
&= \vec{x}^i_{\mathrm{IMU}} + R^i_b \vec{b}^b_{\mathrm{IG}} && (6.36)
\end{aligned}
$$

differentiating on both sides and applying the Coriolis law from equation 2.4 yields

$$
\begin{aligned}
\dot{\vec{x}}^i_{\mathrm{GPS}} &= \dot{\vec{x}}^i_{\mathrm{IMU}} + \dot{R}^i_b \vec{b}^b_{\mathrm{IG}} + R^i_b \dot{\vec{b}}^b_{\mathrm{IG}} \\
&= \dot{\vec{x}}^i_{\mathrm{IMU}} + R^i_b \Omega^b_{ib} \vec{b}^b_{\mathrm{IG}} && (6.37)
\end{aligned}
$$

where in the second equality it has been considered that $\dot{\vec{b}}^b_{\mathrm{IG}} = 0$ because the vector is constant in the body-fixed frame. Differentiating again yields

$$
\begin{aligned}
\ddot{\vec{x}}^i_{\mathrm{GPS}} &= \ddot{\vec{x}}^i_{\mathrm{IMU}} + \dot{R}^i_b \Omega^b_{ib} \vec{b}^b_{\mathrm{IG}} + R^i_b \dot{\Omega}^b_{ib} \vec{b}^b_{\mathrm{IG}} + R^i_b \Omega^b_{ib} \dot{\vec{b}}^b_{\mathrm{IG}} \\
&= \dot{\vec{x}}^i_{\mathrm{IMU}} + R^i_b \Omega^b_{ib} \Omega^b_{ib} \vec{b}^b_{\mathrm{IG}} && (6.38)
\end{aligned}
$$

where in the second equality the assumption that in our model the angular rate vectors are constant (and thus $\dot{\Omega}^b_{ib} = 0$) has been exploited. Rotating back to the body-fixed frame yields

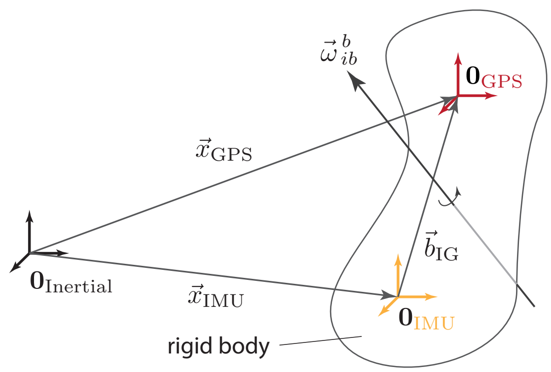

Figure 6.8: Graphical representation of the GNSS and INS body-fixed coordinate frame

$$
\begin{aligned}
R_i^b \ddot{\vec{x}}_{\mathrm{GPS}}^{\,i} &= R_i^b \left(\ddot{\vec{x}}_{\mathrm{IMU}}^{\,i} + + R_b^i \Omega_{ib}^b \Omega_{ib}^b \vec{b}_{\mathrm{IG}}^{\,b} \right) \\
\vec{a}_{\mathrm{GPS}}^{\,b} &= \vec{a}_{\mathrm{IMU}}^{\,b} + \Omega_{ib}^b \Omega_{ib}^b \vec{b}_{\mathrm{IG}}^{\,b}
\end{aligned}
\tag{6.39}
$$

which gives the desired relationship between the two accelerations in the body-fixed frame. In order to express the acceleration in our reference body-fixed frame (here denoted by $\mathbf{0}_{\mathrm{GPS}}$), one has to add the second term on the right-hand side of equation 6.39 to the INS-referred acceleration $\vec{a}_{\mathrm{IMU}}^{b}$ in our acceleration measurement model in equation 6.24.

Correction for the sensor misalignment

Besides different positioning of the sensor plates, another discrepancy may lie in the heterogeneous orientation of the two coordinate frames. The GNSS-centered coordinate frame has its X-axis aligned as the $\vec{b}_{12}$ baseline vector defined as the line passing through the two phase centers of the two GNSS antennas, whereas the INS sensor plate is aligned according to the accelerometers and gyroscope placement. Nevertheless this misalignment is fixed and remains constant due to the rigid body assumption, and it is simply corrected by pre-rotating both the acceleration and angular rate measurements.

If one defines the rotation from the INS-oriented to the GNSS-oriented body-fixed frame using Euler attitude angles (see section 2.2.3), the rotation matrix can be defined as

$$
R_{\mathrm{IMU}}^{\mathrm{GPS}} = R_1(\Delta\varphi_{\mathrm{GI}}) R_2(\Delta\theta_{\mathrm{GI}}) R_3(\Delta\psi_{\mathrm{GI}}) \tag{6.40}
$$

where $\Delta\varphi_{\mathrm{GI}}$, $\Delta\theta_{\mathrm{GI}}$ and $\Delta\psi_{\mathrm{GI}}$ are the Euler attitude angles that describe the rotation from the INS-oriented to the GNSS-oriented body-fixed frame. In order to provide the inertial measurement in the latter frame, one has simply to apply the just defined rotation matrix to the acceleration and angular rate measurements as:

$$\vec{f}^{\,b}_{\text{GPS}} = R^{\text{GPS}}_{\text{IMU}} \vec{f}^{\,b}_{\text{IMU}} \tag{6.41}$$

$$\vec{\omega}^{\,b}_{ib,\,\text{GPS}} = R^{\text{GPS}}_{\text{IMU}} \vec{\omega}^{\,b}_{ib,\,\text{IMU}} \tag{6.42}$$

where $\vec{f}^{\,b}$ and $\vec{\omega}^{b}_{ib}$ are the acceleration and angular rate inertial measurements, respectively.

6.3 Tight coupling results

In the following, the results of the tight coupling algorithm shall be presented. As presented in section 5.1, the algorithm made use of carrier phase, pseudorange and Doppler measurements recorded with low-cost GNSS receivers and of acceleration and angular rate measurements from a low-cost IMU composed of microelectromechanical system (MEMS) sensors. In addition, in order to perform RTK positioning, carrier phase and pseudorange measurements coming from a virtual reference station (VRS) have been used. The position of this VRS is up to 3km away from the track driven by the car. All the estimated parameters have been calculated with the extended Kalman Filter approach described in chapter 5.

The position estimate is shown on a satellite image in Figure 6.9. The tightly coupled position estimation (orange track) is plotted against a reference solution (green track). The white arrows advise for the vehicle's direction of motion. The route has took place in Wolfsburg (Germany), and the trip included urban environments and a 300 meter long tunnel driven two times (upper right enlargement).

Figure 6.10 shows the horizontal position error in the local North and East components of the navigation frame w.r.t. the reference solution over time. As one can see from the plot, there is an initial error of about half a meter on the East component and about 1.4 meter in the North component. However, we think that a good part of this offset is caused by the different positioning of the origin point of the reference w.r.t. our solution (see section 6.2.3). Nevertheless, the variability of the error over time suggests an incorrect fixing of the integer ambiguities as a possible cause of a smaller part of the offset. The unsuccessful initial fixing could be caused by the unmodeled carrier phase multipath error, that strongly influenced on one hand the convergence speed of the float Kalman filter and on the other hand the validity of the baseline drift parameter. All in all, the filter algorithm is able to handle the initial offset and, thanks also to the support of the inertial sensor, to bound the error during the whole trip.

Figure 6.11 depicts the heading attitude angle estimation over time for both our tightly coupled and reference solution. Thanks to the dual GNSS antenna setup and the inertial sensor, the vehicle's attitude can be estimated very precisely. The enlargement shows the heading estimation during the first tunnel

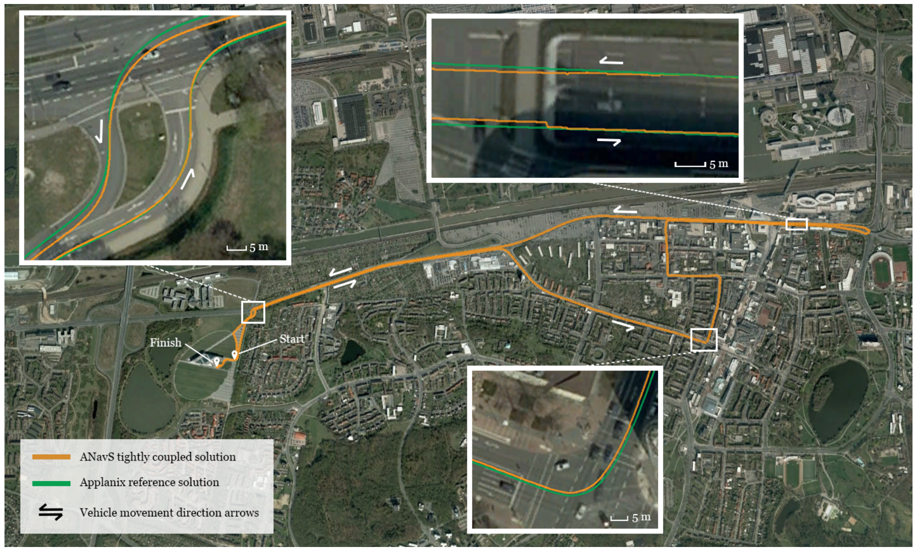

Figure 6.9: Google Earth plot of vehicle trajectory w.r.t. a reference solution

transit, where the satellite signal is completely absent. As one can see, the estimation remains quite accurate even for long GNSS signal interruptions (the first trip lasted for about 30 seconds).

The cumulative distribution of the heading error is depicted in Figure 6.12. The statistics show that we are able to bound the error below one degree up to the 3σ value, namely 99,79% of the time.

Figure 6.13 shows the estimation of the horizontal velocities in the local North and East components. As one can see, apart from the errors during the two tunnel transits induced by incorrect bias estimation due to absence of GNSS measurements, the velocity has been estimated quite accurately.

Finally, we wanted to give a motivation about estimating the code phase multipath error. In urban environments, as the one depicted in Figure 6.14, the multipath parameter can become relatively high. In the latter figure it is shown also the multipath parameter estimation during a phase where the car was standing at a traffic light (the location of the vehicle that refers to the MP plot is depicted with a white dot). As one can see, the multipath parameter can grow up to 10 meters in urban environments and shows some temporal correlation that validates its estimation in our Kalman filter approach.

In conclusion we can say that we are able to perform GNSS/INS tight coupling with an extended Kalman Filter in urban environments with high multipath scenarios even under street tunnels under total absence of GNSS signal reception using low-cost GNSS and INS sensors. Relying strongly on carrier phase measurements, where the correct fixing of the integer ambiguity is an essential requirement for centimeter-level absolute positioning, the position accuracy is strongly related to the the latter assumption. Even if we didn't succeed in fix-

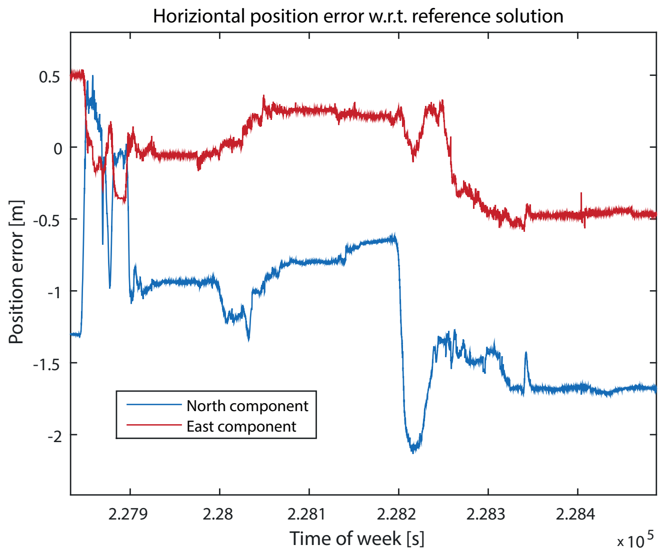

Figure 6.10: Horizontal position error w.r.t. the reference solution in the local North and East components

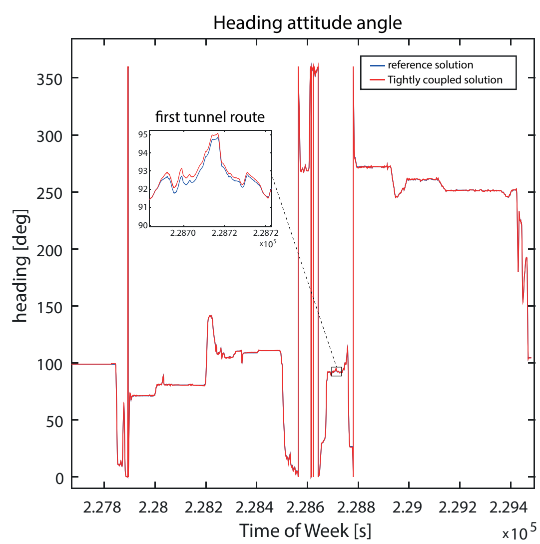

Figure 6.11: Heading estimation time plot, confront with reference solution

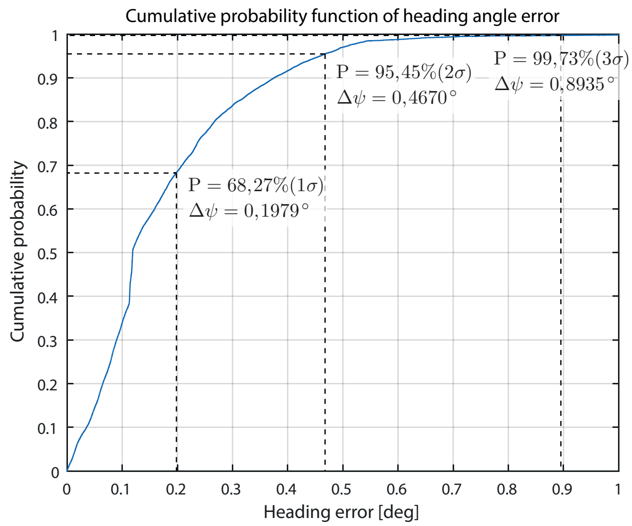

Figure 6.12: Cumulative distribution function of the heading error w.r.t the reference solution

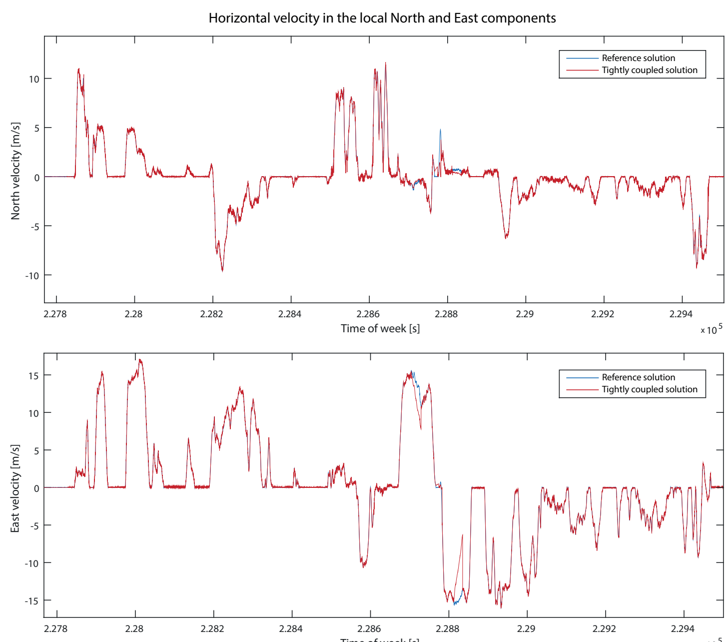

Figure 6.13: Velocity time plot along the local North and East coordinates, respectively; confront with reference solution

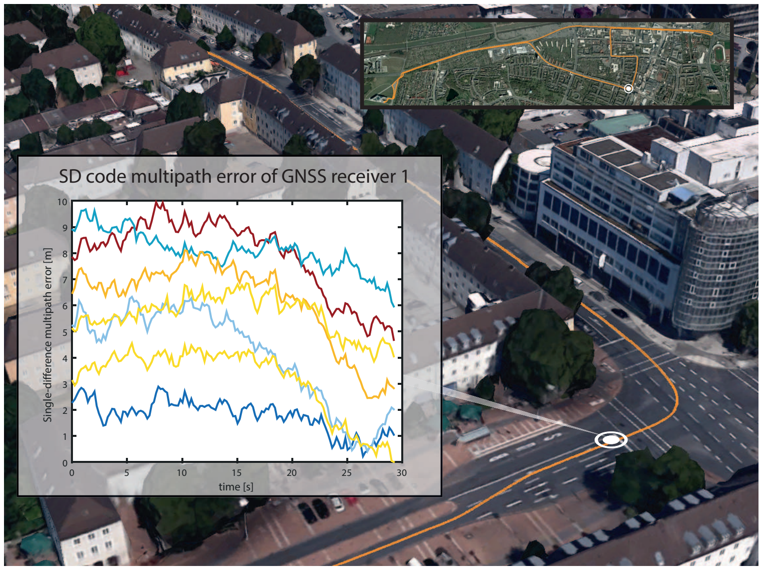

Figure 6.14: GNSS receiver 1 single difference code multipath error estimation in urban environment while vehicle is standing at a traffic light

ing correctly the ambiguities, we have shown that the positioning error remains bounded around the meter level. Thanks to the dual GNSS antenna approach, we are able to estimate the vehicle's attitude very precisely, shrinking the error in the heading angle below one degree under the 3σ value.

Appendix A

Nomenclature

A.1 Basic Quantities and Physics

$\mathbb{N}$	Natural numbers $(1, 2, 3, \ldots)$
$\mathbb{Z}$	Integer numbers $(\ldots, -2, -1, 0, 1, 2, \ldots)$
$\mathbb{R}$	Real numbers
$\mathbb{C}$	Complex numbers
$j = \sqrt{-1}$	Imaginary unit
$\Re(z),\ \Im(z)$	Real and imaginary part of variable z
$\dot{x} = dx/dt$	First derivative of $x(t)$ w.r.t. to time
$\ddot{x} = d^2x/dt^2$	Second derivative of $x(t)$ w.r.t. to time
$\frac{\partial}{\partial x_1} f(x_1, x_2, \ldots)$	First partial derivative of function $f(x_1, x_2, \ldots)$
$\vec{F}$	Force [N]
$\mathcal{P}$	Power [W]
$\mathcal{E}$	Energy [J]
$c = 299792458$ m/s	Speed of light [m/s]

A.2 Vectors, Matrices

$\rho, \xi, \eta, \ldots$	Vectors in any space (no geometrical meaning)
$A, B, \ldots$	Matrices (capital letters)
A^T	Transpose matrix
$\vec{r}$	Geometrical vector (up to three dimensions)
$\mathbb{1}$	Identity matrix
$a \cdot b$	Dot product of vectors a and b (i.e. $a \cdot b = a^T b = \langle a, b \rangle$)
$a \wedge b$	Cross product of vectors a and b
$\lVert a \rVert$	Euclidean norm of a vector ($= \sqrt{\sum_i a_i^2}$)
$\lVert a \rVert_W^2$	Squared norm with metric W ($= a^T W a$)
$a \perp b$	Orthogonality between vector a and b

$\det(A)$	Determinant of matrix A
$\mathrm{grad} f(x)$	Gradient of function $f(x)$ (i.e. $\mathrm{grad}(f) = (\frac{\partial f}{\partial x_1}, \frac{\partial f}{\partial x_2}, \ldots)^T$)
$\mathrm{Trace}[A]$	Trace of matrix A ($= \sum_i a_{ii}$)
$R_1(\alpha) = \begin{pmatrix} 1 & 0 & 0 \\ 0 & \cos(\alpha) & -\sin(\alpha) \\ 0 & \sin(\alpha) & \cos(\alpha) \end{pmatrix}$	Rotation matrix with the x-axis as the rotation axis
$R_2(\beta), R_3(\gamma)$	Rotation matrices w.r.t. the y- and z-axis

A.3 Positioning

x^k	Quantity x referring to satellite k
x_i	Quantity x referring to receiver/ground station i
K	Number of satellites
$\vec{r}_i$	Position vector of receiver i [m]
$\vec{r}^{\,k}$	Position vector of satellite k [m]
δ_i	Clock offset of receiver i [s]
ρ_i^k	Pseudorange of satellite k to receiver i [m]
ρ_i	Vector containing all pseudoranges ($= (\rho_i^1, \ldots, \rho_i^K)^T$)
ϕ_i^k	Phase measurement [cycles]
ϕ_{ij}^k	Single difference phase measurements ($\phi_{ij}^k = \phi_i^k - \phi_j^k$) [cycles]
ϕ_{ij}^{kl}	Double difference phase measurements ($\phi_{ij}^{kl} = (\phi_i^k - \phi_j^k) - (\phi_i^l - \phi_j^l)$) [cycles]
Φ_i	Vector containing all phase measurements of receiver i
N_i^k	Integer ambiguity [ ]
$\vec{e}_i^{\,k}$	Unit vector pointing from satellite k to the receiver i
e_x^k, e_y^k, e_z^k	Components of the unit vector $\vec{e}^{\,k}$
$H = \begin{pmatrix} (\vec{e}^{\,1})^T & 1 \\ \vdots & \vdots \\ (\vec{e}^{\,K})^T & 1 \end{pmatrix}$	Geometry matrix
E	Elevation angle [rad]
ξ_i	Space-time vector, i.e. vector containing the (ECEF-) position and clock offset of receiver i ($\xi_i = (x_i, y_i, z_i, c\delta_i)^T$) [m]
χ_i	Time-derivative of the space-time vector ξ_i, i.e. vector containing the velocity and clock drift of receiver i ($\chi_i = (v_{i,x}, v_{i,y}, v_{i,z}, c\dot{\delta}_i)^T$) [m/s]
I_i^k	Ionospheric delay [m]
T_i^k	Tropospheric delay [m]
f_D	Doppler shift [Hz]
R_e	Radius of the earth [m]

A.4 Random Variables, Estimation

$p_X(x)$	Probability density function of r.v. X (short $p(x)$)
$p_{X\|Y}(x\|y)$	Conditional probability density function of r.v. X given r.v. Y
$\Phi_X(x) = \int_{-\infty}^{x} p_X(y)dy$	Cumulative distribution function of r.v. X
$\Phi(x) \prec \Phi_O(x)$	Distribution over-bound (i.e. cdf Φ is overbound by Φ_O)
$\mathcal{E}[x]$	Expected value of x
$\mathrm{var}[x]$	Variance of x
$\hat{x}$	Estimate of quantity x
C	Covariance matrix ($C_x = \mathcal{E}\big[\big(x - \mathcal{E}[x]\big)\big(x - \mathcal{E}[x]\big)^T\big]$)
$W = C^{-1}$	Weighting matrix v
$\mathcal{N}_0$	Noise density [W/Hz]
ε, η, n	Noise (could be time-continuous or -discrete functions of time)
$\mathcal{A}, \bar{\mathcal{A}}$	Event and the corresponding complementary event
$\mathcal{A} \vee \mathcal{B}$	Event A or event B
K_t	Kalman gain at time-step t
Φ_t	State-transition matrix at time-step t
H_t	Measurement matrix at time-step t

A.5 Signal Processing

$u \oplus v$	Modulo 2 addition ($0 \oplus 0 = 1 \oplus 1 = 0$, $0 \oplus 1 = 1 \oplus 0 = 1$)
$x_{t-1},\ x_t,\ x_{t+1}, \ldots$	Discrete-time signal
$\mathrm{sinc}(x) = \sin(x)/x$	Sinus cardinalis of x
$T_s = 1/f_s$	Sampling interval [s] and sampling rate [Samples/s]
$T_c = 1/f_c$	Chip length [s] and chipping rate [Chips/s]
ω_c	Carrier frequency [rad/s]
T_i	Predetection integration interval [s]
$p(t)$	Rectangular pulse ($= \mathrm{rect}(x/T_c)$)
b_m	Navigation bit
$C(.)$	Correlation function (of sequences and between received signal and local copy, e.g. Early correlation result: $C_E(\Delta\tau)$)
$R(\tau)$	Autocorrelation function (of signals $R(\tau) = \mathcal{E}[s(t)s(t+\tau)]$)
$S(f) = \int_{-\infty}^{\infty} R(\tau) e^{-j2\pi f\tau} d\tau$	Power spectral density
$\bar{f} = \left(\int f^2 \left\|S(f)\right\|^2 df\right)^{1/2}$	Gabor bandwidth
B_L	Filter loop bandwidth [Hz]
$\mathrm{cosb}_{(m,n)}(t) = \mathrm{sign}\big(\cos(2\pi t/T_s)\big)$	BOC-signal (cosine-phased)
$\mathrm{sinb}_{(m,n)}(t) = \mathrm{sign}\big(\sin(2\pi t/T_s)\big)$	BOC-signal (sine-phased)
$\delta_{i,j}$	Kronecker delta ($\delta_{i,j} = 1$ if $i = j$, and 0 otherwise)
$F(.)$	Transformed function $f(t)$ (e.g. $F(z), F(w), F(s)$)

Bibliography

[1] C. Jekeli, *Inertial Navigation Systems with Geodetic Applications.* Bod Third Party Titles, 2001.

[2] A. Noureldin, T. B. Karamat, and J. Georgy, *Fundamentals of INS, GPS and Their Integration.* Springer Science & Business Media, 2012.

[3] J. L. Junkins and M. D. Shuster, "The geometry of the euler angles," *Journal of the Astronautical Sciences*, vol. 41, no. 4, pp. 531–543, 1993.

[4] European Space Agency, "What is Galileo?." `http://www.esa.int/Our_Activities/Navigation/The_future_-_Galileo/What_is_Galileo`, 2015. [Online; accessed 20-Aug-2015].

[5] P. Misra and P. Enge, *Global positioning system: signals, measurements, and performance.* Ganga-Jamuna Press, 2006.

[6] I. G. Petrovski, *GPS, GLONASS, Galileo, and BeiDou for Mobile Devices: From Instant to Precise Positioning.* Cambridge University Press, 2014.

[7] E. Kaplan and C. Hegarty, *Understanding GPS: principles and applications.* Artech house, 2005.

[8] L. Serrano, D. Kim, and R. B. Langley, "Multipath adaptive filtering in GNSS/RTK-based machine automation applications," in *Position Location and Navigation Symposium (PLANS), 2010 IEEE/ION*, pp. 60–69, IEEE, 2010.

[9] P. Henkel and M. Iafrancesco, "Tightly coupled position and attitude determination with two low-cost GNSS receivers," in *The eleventh IEEE Symposium on Wireless Communication System, Barcelona*, 2014.

[10] C. Günther and P. Henkel, "Integer ambiguity estimation for satellite navigation," *Signal Processing, IEEE Transactions on*, vol. 60, no. 7, pp. 3387–3393, 2012.

[11] P. J. Teunissen, "The least-squares ambiguity decorrelation adjustment: a method for fast GPS integer ambiguity estimation," *Journal of Geodesy*, vol. 70, no. 1-2, pp. 65–82, 1995.

[12] C. Hide and T. Moore, "GPS and low cost INS integration for positioning in the urban environment," in *ION GNSS 18th International Technical Meeting of the Satellite Division, Long Beach, CA*, 2005.

[13] Y. Li, J. Wang, C. Rizos, P. Mumford, and W. Ding, "Low-cost tightly coupled GPS/INS integration based on a nonlinear kalman filtering design," in *Proceedings of ION National Technical Meeting*, pp. 18–20, Citeseer, 2006.

[14] J. Georgy, A. Noureldin, M. J. Korenberg, and M. M. Bayoumi, "Low-cost three-dimensional navigation solution for RISS/GPS integration using mixture particle filter," *Vehicular Technology, IEEE Transactions on*, vol. 59, no. 2, pp. 599–615, 2010.

[15] P. Groves, *Principles of GNSS, Inertial, and Multisensor Integrated Navigation Systems, Second Edition:*. GNSS/GPS, Artech House, 2013.

[16] P. Henkel and C. Günther, "Attitude determination with low-cost GPS/INS," in *Proc. of the 26-th Intern. Techn. Meeting of the Satellite Division of the Institute of Navigation (ION GNSS+), Nashville, TN, USA*, pp. 2015–2023, 2013.

[17] S. Belongie, "Rodrigues' rotation formula." From MathWorld–A Wolfram Web Resource, created by Eric W. Weisstein `http://mathworld.wolfram.com/RodriguesRotationFormula.html`. [Online; accessed 8-Sep-2015].